

# Efficient Cocatalyst-Free Piezo-Photocatalytic Hydrogen Evolution of Defective $\text{BaTiO}_{3-x}$ Nanoparticles from Seawater

Yue Jiang,\* Cui Ying Toe, Sajjad S. Mofarah, Claudio Cazorla, Shery L.Y. Chang, Yanting Yin, Qi Zhang, Sean Lim, Yin Yao, Ruoming Tian, Yuan Wang, Tasmia Zaman, Hamidreza Arandiyani, Gunther G. Andersson, Jason Scott, Pramod Koshy, Danyang Wang,\* and Charles C. Sorrell\*



Cite This: *ACS Sustainable Chem. Eng.* 2023, 11, 3370–3389



Read Online

ACCESS |



Metrics & More



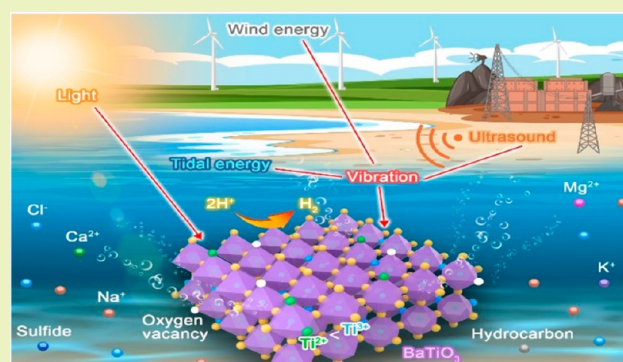
Article Recommendations



Supporting Information

**ABSTRACT:** Hydrogen is a promising fossil-fuel alternative fuel owing to its environmentally neutral emissions and high energy density. However, the need for purified water and external power are critical hindrances to the implementation of hydrogen production. The present work demonstrates the potential to overcome these shortcomings through piezo-photocatalysis of seawater using defective  $\text{BaTiO}_{3-x}$  (BTO) nanoparticles. This material was made piezoelectrically active by a straightforward annealing process under different atmospheres, including  $\text{O}_2$ ,  $\text{N}_2$ , Ar, or  $\text{H}_2$ , the latter of which caused  $\text{Ti}^{4+} \rightarrow \text{Ti}^{(4-x)+}$  multiple reductions and structural distortions that stabilize piezoelectric tetragonal domains. A suite of experimental techniques was employed to reveal the effects of reduction on the energy band structure. A substantial piezoelectric effect and the presence of self-polarization were confirmed by piezoresponse force microscopy, while simulation work clarified the role of vibrations on band bending deriving from the self-polarization. The hydrogen evolution through photocatalysis, piezocatalysis, and piezo-photocatalysis over the defective  $\text{BaTiO}_{3-x}$  nanoparticles was characterized with deionized (DI) water, simulated seawater, and natural seawater. A promising HER with a rate of  $132.4 \mu\text{mol/g/h}$  was achieved using DI water through piezo-photocatalysis without a cocatalyst. In contrast, a substantial HER rate of  $48.7 \mu\text{mol/g/h}$  was obtained for natural seawater, despite the deleterious impact of dissolved ions. The present work offers new perspectives for large-scale green  $\text{H}_2$  production using abundant natural resources with a conventional piezoelectric material that is readily available but still affected by the ions dissolved in seawater.

**KEYWORDS:** piezo-photocatalysis, seawater splitting,  $\text{BaTiO}_3$ , hydrogen evolution reaction, defect chemistry



## INTRODUCTION

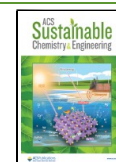
A hydrogen economy is receiving greater attention as a potential means of dealing with climate change and securing a sustainable clean energy resource. Hydrogen as a sustainable energy carrier is a promising alternative to fossil fuels owing to its environmentally neutral emissions and high energy density.<sup>1</sup> At present, most hydrogen generation is from natural gas by steam reforming using the water–gas shift reaction.<sup>2</sup> However, water splitting is the ideal pathway to achieve efficient hydrogen production owing to its cyclic production–oxidation reactions and the storage/transport capacities in both liquid and gas forms. The principal alternative to the steam reforming is electrolysis although it has the disadvantages of requiring an external power input, the necessity of separation of the  $\text{H}_2$  produced at the cathode by the hydrogen evolution reaction (HER) and the  $\text{O}_2$  produced at the anode by the oxygen evolution reaction (OER), the necessity of the use of purified water, and limited freshwater supplies. Although electrolysis exhibits  $\sim 80\%$  efficiency, this can be increased with the use of

electrocatalysts, photocatalysts, piezocatalysts, or thermocatalysts.<sup>3</sup> Although the associated catalytic processes require energy inputs in the laboratory setting, they can be green and sustainable on the industrial scale through the use of solar cells, sunlight, wind/tide, and geothermal/concentrated sunlight, respectively. Further advantages may be gained through the combination of two or even more of these catalytic processes.<sup>4</sup> Although countries such as Australia are poised to leverage all of these processes owing to its high sunlight flux, large land mass, and extensive shoreline, it has the disadvantage

Received: November 3, 2022

Revised: December 28, 2022

Published: January 13, 2023



of limited supplies of freshwater. This situation highlights the importance of developing means of the splitting of seawater.

Seawater is the most abundant aqueous feedstock on earth but there are three principal challenges that will determine the feasibility of direct seawater splitting. First, the similarity of the electrochemical potentials of the OER at 1.23 eV and the chlorine evolution reaction (CER) at 1.36 eV raises the possibility of the production of chlorine-containing products (e.g., chlorine gas, hypochlorous acid, or hypochlorite).<sup>5</sup> Second, the presence of such scavengers in seawater, e.g., the hole scavenger  $\text{Cl}^-$ , is disadvantageous because they can compete with the HER and OER for catalytically generated electrons and holes, respectively. The competition between HER and OER is affected by the electron reactions. That is, the formation of chlorine gas (CER), hypochlorous acid, and hypochlorite is a two-electron reaction and so is dominated by the kinetics, whereas the OER is a four-electron reaction and so is dominated by equilibrium thermodynamics.<sup>63</sup> A further consideration is the concentration of  $\text{Cl}^-$ , where low concentrations leverage the lower CER potential compared to that of OER, which would enhance the efficiency of the complementary HER reaction. In contrast, high concentrations can hinder these reactions owing to the generation of hypochlorite; although, simple blockage of active sites also is possible. Third, the microorganisms and other organic matter present in seawater could alter the catalytic process, leading to undesirable side-reactions, or foul and deactivate the catalyst. The preceding risks clarify the desirability of using DI water for water splitting but they also highlight the desirability of developing catalysts for green, sustainable, efficient, and reliable seawater splitting.

One approach to hydrogen production is solar-driven seawater splitting using different semiconductor photocatalysts. Simamora et al.<sup>6</sup> used Degussa P25  $\text{TiO}_2$  and UV irradiation to contrast the photocatalytic  $\text{H}_2$  evolution rates for DI water (8.5  $\mu\text{mol/g/h}$ ) and simulated seawater (3.1  $\mu\text{mol/g/h}$ ). They also observed that the addition of a  $\text{CuO}$  cocatalyst increased the range of absorption spectrum and consequent  $\text{H}_2$  evolution rate to 15.7  $\mu\text{mol/g/h}$ . In another study, Peng et al.<sup>7</sup> prepared  $\text{CdS}/\text{TiO}_2$  nanocomposites for both DI water and simulated seawater splitting and demonstrated respective  $\text{H}_2$  evolution rates of 306.3 and 456.6  $\mu\text{mol/g/h}$ . In this work, low concentrations of sacrificial agents (0.1 mol/L  $\text{Na}_2\text{S}$  + 0.1 mol/L  $\text{Na}_2\text{SO}_3$ ) were added in order to reduce the recombination of electrons and holes and thereby accelerate the HER.<sup>8</sup> Consequently, the introduction of anions appears to have achieved the intended aim, thus suggesting that the beneficial effect of suitable concentrations of  $\text{S}^{2-}/\text{SO}_3^{2-}$  dominated the deleterious effect of  $\text{Cl}^-$ . The summary offered in Table S1 indicates that photocatalytic seawater splitting is impacted by a range of issues, including materials design complexity, necessity of the use of scavengers, and limited quantum efficiencies.<sup>4</sup>

A second approach to hydrogen production is via piezocatalysis, although this has been applied only to DI water at present.<sup>9</sup> This relatively new mechanism is based on the principle of converting cyclic mechanical energy into chemical energy. Such mechanical vibration exists in several easily accessed forms, including tides, as a byproduct of wind-generated power, and sound/ultrasound systems. In this process, the piezo-potential induced by mechanical vibration causes electronic band bending, which directs the internal charge carrier flow to the catalyst surface, thereby facilitating the catalytic reaction. The band bending also can improve the

photogenerated charge carrier separation by shifting the band edges relative to the HER and OER electrochemical potentials, thus improving the photocatalytic activity.<sup>10</sup> Several piezoelectric materials have been explored as promising candidates for piezocatalysis, including  $\text{BaTiO}_3$ ,<sup>4,10,11</sup>  $\text{ZnO}$ ,<sup>12</sup>  $\text{Na}_{0.5}\text{K}_{0.5}\text{NbO}_3$ ,<sup>13</sup>  $\text{BiFeO}_3$ ,<sup>14</sup> and  $\text{Na}_{0.5}\text{Bi}_{0.5}\text{TiO}_3$ .<sup>15</sup> Hong et al.<sup>12</sup> carried out the splitting of DI water with hydrothermally prepared  $\text{ZnO}$  nanofibers at unspecified frequency and power levels. This work revealed a very high  $\text{H}_2$  evolution rate (2192.2  $\mu\text{mol/g/h}$ ) and a notable efficiency of conversion of mechanical energy to chemical energy of  $\sim 18\%$ . You et al.<sup>13</sup> synthesized  $\text{BiFeO}_3$  square nanosheets using a hydrothermal method and obtained a high  $\text{H}_2$  production rate of 124.1  $\mu\text{mol/g/h}$  using ultrasound at an unspecified frequency and 100 W. Tetragonal  $\text{BaTiO}_3$  is a well-known wide-band gap ferroelectric material that has been reported to exhibit both photocatalytic and thermocatalytic functions, although rapid charge carrier recombination hinders its performance.<sup>16</sup> An advantage of tetragonal  $\text{BaTiO}_3$  is that it demonstrates pressure-induced polarization, which allows for the establishment of a dynamic built-in electric field during vibration, viz., the piezoelectric polarization field. The polarization allows the electrons and holes to maintain continuous separation, thus preventing recombination and their consequent mobilization on opposite surfaces, thereby making them available for catalytic hydrogen production.<sup>16</sup> Recently, Su et al.<sup>11</sup> developed porous and structurally defective  $\text{BaTiO}_3$  nanoparticles using a hydrothermal method and investigated the DI water splitting performance. They obtained a high  $\text{H}_2$  evolution rate of 159  $\mu\text{mol/g/h}$  at 40 kHz frequency and unspecified power, which they attributed to the presence of surface strain, associated enhanced polarization, and high surface area.

A third approach is based on the potential for additive effects by combining the two approaches of photocatalysis and piezocatalysis as piezo-photocatalysis of DI water. However, the literature is contradictory in this regard. Wang et al.<sup>17</sup> studied both dye degradation and DI water splitting with hydrothermally synthesized  $\text{ZnSnO}_3$  nanowires through photocatalysis, piezocatalysis, and piezo-photocatalysis. The rhodamine B dye (RhB) degradation efficiency using piezo-photocatalysis was 1.53 and 2.30 times higher than those of photocatalysis and piezocatalysis, respectively. An  $\text{H}_2$  evolution rate of 3882.5  $\mu\text{mol/g/h}$  was obtained by the synergistic piezo-photocatalysis, which was higher than those for photocatalysis (3453.1  $\mu\text{mol/g/h}$ ) and piezocatalysis (3562.2  $\mu\text{mol/g/h}$ ). These results are in line with Xiao et al.,<sup>18</sup> who prepared Ag-decorated  $\text{Na}_{0.5}\text{Bi}_{0.5}\text{TiO}_3\text{-Ba}(\text{Ti}_{0.5}\text{Ni}_{0.5})\text{O}_3$  composite nanopowder by self-propagating high-temperature synthesis. A high  $\text{H}_2$  evolution rate of 450  $\mu\text{mol/g/h}$  was obtained using piezo-photocatalysis, compared to those of photocatalysis (67.75  $\mu\text{mol/g/h}$ ) and piezocatalysis (47.71  $\mu\text{mol/g/h}$ ). In contrast, the previously mentioned work by Su et al.<sup>11</sup> on defective  $\text{BaTiO}_3$  revealed that piezo-photocatalysis exhibited a lower  $\text{H}_2$  evolution rate (103  $\mu\text{mol/g/h}$ ) than that of piezocatalysis (159  $\mu\text{mol/g/h}$ ), although photocatalysis gave nil results. They attributed this to the different charge transfer mechanisms of the two catalyzes. That is, piezocatalysis is driven by the spontaneous polarization/depolarization caused by cyclic compressive stress application/release, respectively, thus establishing a surface piezo-potential. Photocatalysis is inactive owing to insufficient redox potential deriving from the charge carriers. With piezo-photocatalysis, the large number of charge carriers, albeit of low redox potential, becomes sufficient to enhance

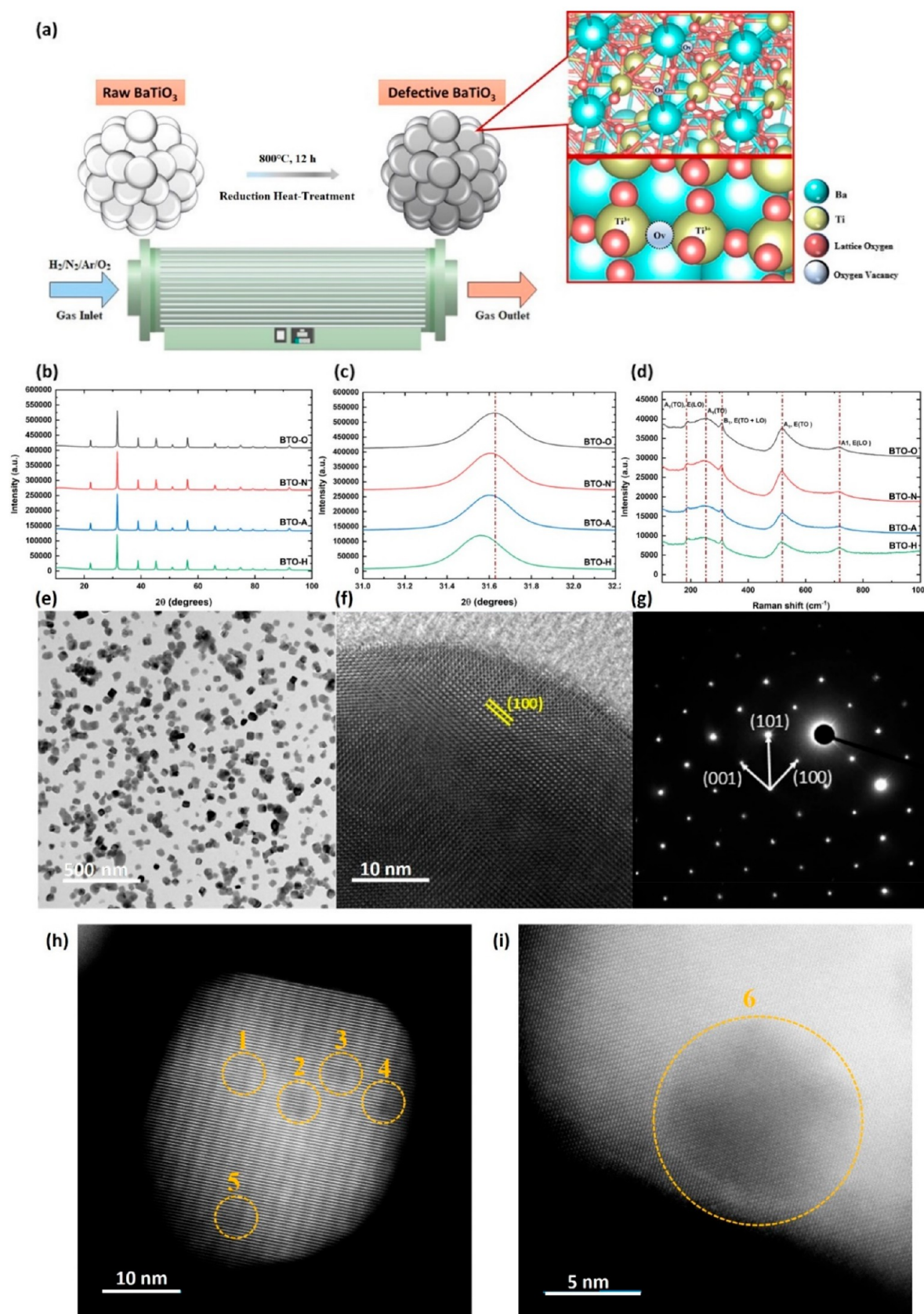


**Figure 1.** Synthesis and characterization of defective BTO nanoparticles. (a) Schematic diagram for synthesis. XRD patterns: (b) range  $10^{\circ}$ – $100^{\circ}$   $2\theta$  (identical pattern scales) and (c) range  $30^{\circ}$ – $35^{\circ}$   $2\theta$  (identical pattern scales). (d) Laser Raman microspectroscopy patterns (identical pattern scales). TEM images of BTO-H: (e) low-magnification bright-field image and (f) high-resolution image. (g) SAED image for BTO-H for (f) HAADF-STEM images of BTO-H: (h) lower magnification image of entire particle (circled regions indicate oxygen-vacancy-rich tetragonal domains) and (i) higher magnification image particle edge.

photocatalysis, but, at the same time, the charge carriers screen the surface potential, thus hampering the water splitting process.

A survey of the literature indicates there are very few studies on piezo-photocatalytic splitting of seawater for H<sub>2</sub> production with ferroelectric nanomaterials. Consequently, the present work presents an initial investigation of seawater splitting using the simultaneously applied piezocatalytic and photocatalytic properties of defective BaTiO<sub>3</sub> nanoparticles (as the model material).<sup>34</sup> The role of structural defects was investigated through annealing in different atmospheres (O<sub>2</sub>, N<sub>2</sub>, Ar, H<sub>2</sub>) in order to impose specific defect chemistries. A critical outcome of this strategy was that reduction generated unique structural distortions that induce self-polarization in the BaTiO<sub>3</sub> nanoparticles. The observed Ti<sup>4+</sup> → Ti<sup>(4-x)+</sup> multiple reductions and charge-compensating oxygen vacancies effectively stabilize these structural features,<sup>19,20</sup> which are graded coherently within a more stoichiometric cubic matrix. Although a previous study<sup>32</sup> adopted a similar approach, viz., production of highly oxygen-deficient BTO nanoparticles through heat-treatment under H<sub>2</sub>, it has the disadvantages of complex sample preparation involving lengthy ultrasonic mixing and the requirement of a vacuum oven as well as modest dye-degradation performance. Furthermore, the hydrogen evolution efficiency was not reported in that work. By contrast, our BaTiO<sub>3</sub> nanoparticles annealed in H<sub>2</sub> showed highly efficient dye degradation of RhB (99% degradation in 30 min) and HER rates of up to 132.4 μmol/g/h over DI water through piezophotocatalysis. More importantly, our defective BTO nanoparticles also render remarkable seawater splitting capability with the HER rates of 63.4 μmol/g/h (simulated seawater) and 48.7 μmol/g/h (natural seawater) without a cocatalyst and scavengers. These data suggest that highly defective and structurally stable BaTiO<sub>3</sub> offers the potential for significant outcomes in large-scale green and sustainable freshwater purification and hydrogen production from seawater.

## RESULTS AND DISCUSSION

**Structural Characterization.** Commercial cubic BaTiO<sub>3</sub> (BTO) nanoparticles (<100 nm) were modified to vary the defect concentrations by heat-treatment in O<sub>2</sub>, N<sub>2</sub>, Ar, or H<sub>2</sub> at 800 °C for 12 h and then cooled to room temperature. The resultant samples were denoted as BTO-O, BTO-N, BTO-A, and BTO-H, respectively. In contrast with the first three, a significant change in color from white to dark gray was observed when the BTO was annealed under H<sub>2</sub>, thus confirming its greater extent of reduction. Schematic details of the synthesis are shown in Figure 1a and described in detail in the Experimental Section. Table S2 in the Supporting Information surveys the previous studies reporting the effects of annealing under reducing conditions for the purpose of increasing the defect concentration. Figure 1b shows that the X-ray diffraction (XRD) patterns of all samples can be indexed to BaTiO<sub>3</sub> crystals.<sup>21</sup> Figure 1c shows that the representative (101) peak for BTO-H exhibits a clear shift to a lower angle, thus suggesting lattice expansion from the previously mentioned Ti reduction (charge compensated by oxygen vacancy formation). The XRD Rietveld refinement data for the BTO structure, which is illustrated in Figure S1a, are shown in Figure S1b. The XRD data reveal that the BTO (200) peak exhibits a shoulder at the lower angles, which is indicative of the (002) to (002) + (200) peak splitting and associated onset of the cubic → tetragonal BTO phase transformation.<sup>21,22</sup>

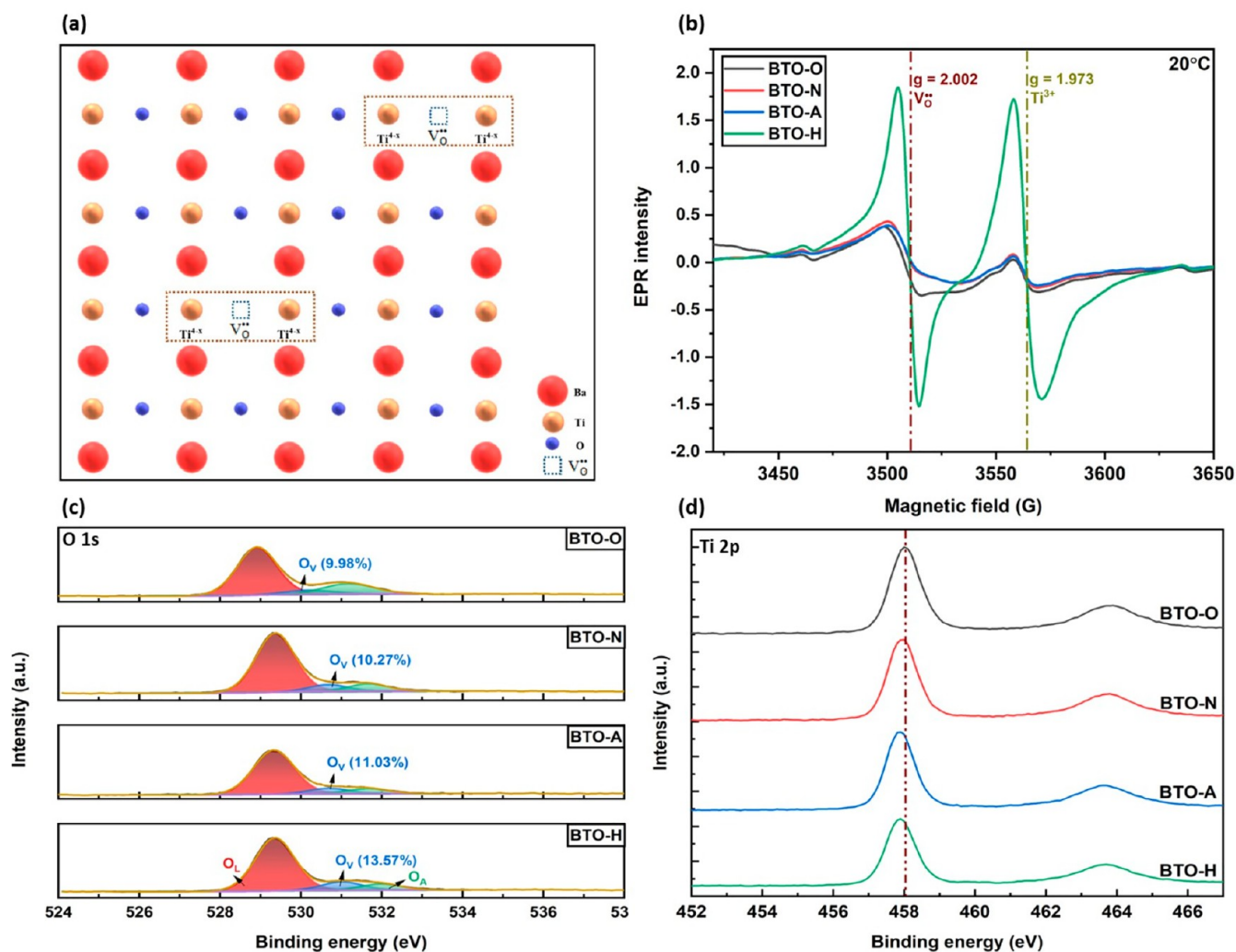
The presence of tetragonal BTO was confirmed by laser Raman microspectroscopy, the spectra for which are shown in

Figure 1d. The main features observed include a small peak at 175 cm<sup>-1</sup> [A<sub>1</sub>(TO), E(LO)], a broad peak centered at 265 cm<sup>-1</sup> [A<sub>1</sub>TO], a relatively sharp peak at 306 cm<sup>-1</sup> [B<sub>1</sub>, E(TO + LO)], a broad sharp peak centered at 520 cm<sup>-1</sup> [A<sub>1</sub>, E(TO)], and a small broad peak centered at 720 cm<sup>-1</sup> [A<sub>1</sub>, E(LO)].<sup>23</sup> It is well-established that cubic BTO is Raman-inactive owing to the isotropic distribution of electrostatic forces around the centrosymmetric Ti<sup>4+</sup> ion.<sup>21,23</sup> The appearance of characteristic Raman peak at 306 cm<sup>-1</sup> confirms the XRD identification of tetragonal BTO. The Raman-active nature of tetragonal BTO derives from the electronic/ionic polarization caused by the off-centered displacement of the Ti<sup>4+</sup> cation within the TiO<sub>6</sub> octahedron,<sup>16</sup> which results in ferroelectric and consequent piezocatalytic behavior.<sup>11</sup>

The nanoparticles were examined in greater detail using transmission electron microscopy (TEM). Figure 1e shows that the BTO-H nanoparticles exhibited monodisperse cuboidal morphologies of typically 30–60 nm size shapes after deagglomeration by 30 min of sonication. The lattice fringes shown in Figure 1f extend throughout the individual grains, thus indicating that they are well-crystallized crystals. The single-crystal nature of the particle, shown in Figure 1f, is demonstrated by the reflections ([001] zone axis) from the selected area electron diffraction (SAED) pattern shown in Figure 1g. The fact that the grain is highly crystalline is demonstrated by the well-defined and bright dots. The tetragonal symmetry is confirmed again by the difference in interplanar spacing of the (001) plane (0.402 nm) and (100) plane (0.400 nm).<sup>24</sup>

The structural homogeneity of BTO-H was examined using high-angle annular dark-field scanning transmission electron microscopy (HAADF-STEM). Part h and i of Figure 1 reveal regions of dark shading that are consistent with enriched oxygen vacancy concentrations. The continuous lattice fringes indicate that these domains are structurally coherent across the graded interface with the lighter matrix. These darker domains, which indicate a lower average atomic density, correspond to tetragonal BTO, which is stabilized by the Ti<sup>4+</sup> → Ti<sup>(4-x)+</sup> multiple reduction/expansion and charge-compensating oxygen vacancies, the dual presence of which is confirmed by the subsequent X-ray photoelectron spectroscopy (XPS) data. This identification is supported by other work that correlates the stabilization of tetragonal BTO with increasing oxygen vacancy concentrations.<sup>19,20</sup>

The structural and chemical characteristics of the BTO samples were further examined by scanning electron microscopy (SEM), energy dispersive spectroscopy (EDS), laser diffraction, and the Brunauer–Emmett–Teller (BET) technique. The SEM images of Figure S3 show that the annealed nanoparticles are agglomerated into micron-sized spheres. However, Figure S1c reveals that sonication for 10 min was sufficient to convert most of the soft agglomerates into the monodisperse particles apparent in Figure 1e. The EDS elemental mapping clearly indicates the presence of Ba, Ti, and O elements, which are uniformly distributed in the nanoparticles. The Brunauer–Emmett–Teller (BET) data for specific surface areas, pore volumes, and average pore sizes are given for the different nanoparticles in Table S3. These data do not show clear correlations between the three sets of data, indicating that the macroscopic pore features are not responsible for the progressively increased surface areas. That is, since the ionic radii of oxygen and nitrogen are within 5% of one another,<sup>25</sup> then it is likely that the surface area represents a measure of the access of a nitrogen ion to an oxygen vacancy. Consequently, the



**Figure 2.** Defect and chemical analyses of BTO nanoparticles. (a) Schematic of hypothetical defect structures (bulk). (b) Room-temperature EPR spectra (bulk, subsurface, surface). (c) O 1s XPS spectra (subsurface) and (d) Ti 2p XPS spectra (surface). The binding energies of XPS peaks were obtained by referencing the C 1s line to 284.8 eV.

surface area represents an alternative means of assessing the oxygen vacancy concentration ( $[V_{\text{O}}^{\bullet\bullet}]$ ). This relation is further illustrated in Figure S2, which reveals clear correlation between the surface area and the  $[V_{\text{O}}^{\bullet\bullet}]$  determined by XPS (Table S4). Further, these data suggest that the effectiveness of the different atmospheres in chemical reduction is in the expected order:

BTO-O (negatively charged O) < BTO-N (negatively charged N) < BTO-A (neutral Ar)  $\ll$  BTO-H (positively charged H)

Since Figure 1h,i indicates that the distribution of the oxygen-vacancy-stabilized tetragonal domains is inhomogeneous, then the parallel trends revealed in Figure S2 suggest that the oxygen vacancies are homogeneously distributed across the surfaces of the grains and that the tetragonal domains are volumetric and are not limited only to the subsurface.

As illustrated in Figure S1a, which is indicated as a simplified projection in Figure 2a, BTO has a typical perovskite structure ( $\text{ABO}_3$ ), which occurs as both cubic (space group  $Pm\bar{3}m$ ) and tetragonal (space group  $P4mm$ ) polymorphs, where  $\text{Ba}^{2+}$  occupies the A site and  $\text{Ti}^{4+}$  occupies the B site. As what effectively is  $\text{BaTiO}_{3-x}$  has intrinsic oxygen vacancies (assuming ionic charge compensation), the application of  $\text{O}_2$  probably decreased this concentration while the application of the

reducing atmospheres ( $\text{N}_2$ , Ar, and  $\text{H}_2$ ) increased it. These atmospheres increase the formation of oxygen vacancies generated by electron migration, viz., polarons.<sup>26</sup> That is, the Ti reduction is caused by electron localization on the Ti ions adjacent to the vacancies, thereby forming a  $\text{Ti}^{4-x}\text{-V}_{\text{O}}^{\bullet\bullet}$  dipole.<sup>26</sup> The room-temperature electron paramagnetic resonance (EPR) scan for the defective BTO in Figure 2b reveals signals at  $g = 2.002$ , assigned to surface  $\text{V}_{\text{O}}^{\bullet\bullet}$ , and at  $g = 1.973$ , assigned to the  $\text{Ti}^{3+}\text{-V}_{\text{O}}^{\bullet\bullet}\text{-Ti}^{3+}$  complex.<sup>10,27,28</sup> The BTO-H exhibits significantly more intense peaks than those of the other three samples, echoing the greatest oxygen concentration as shown Figure S2. In order to confirm the assignments of these peaks, the EPR was done at 70 °C, as shown in Figure S4. While the faster diffusion of the electrons at the higher temperature is consistent with the observed signal attenuation,<sup>29</sup> the maintenance of the  $g$  values confirms that they do not indicate anomalous phenomena and hence are as assigned. Finally, while the progressive  $\text{Ti}^{4+} \rightarrow \text{Ti}^{(4-x)+}$  reductions are feasible for  $\text{H}_2$  reduction, no signal for  $\text{Ti}^{2+}$  and  $\text{Ti}^0$  is visible because they are EPR-inactive.<sup>30</sup>

Parts c and d of Figure 2 show the X-ray photoelectron spectroscopy (XPS) spectra for the BTO nanoparticles. The O 1s XPS spectra of BTO nanoparticles can be deconvoluted into three peaks centered at 529.6, 530.9, and 531.9 eV, which are

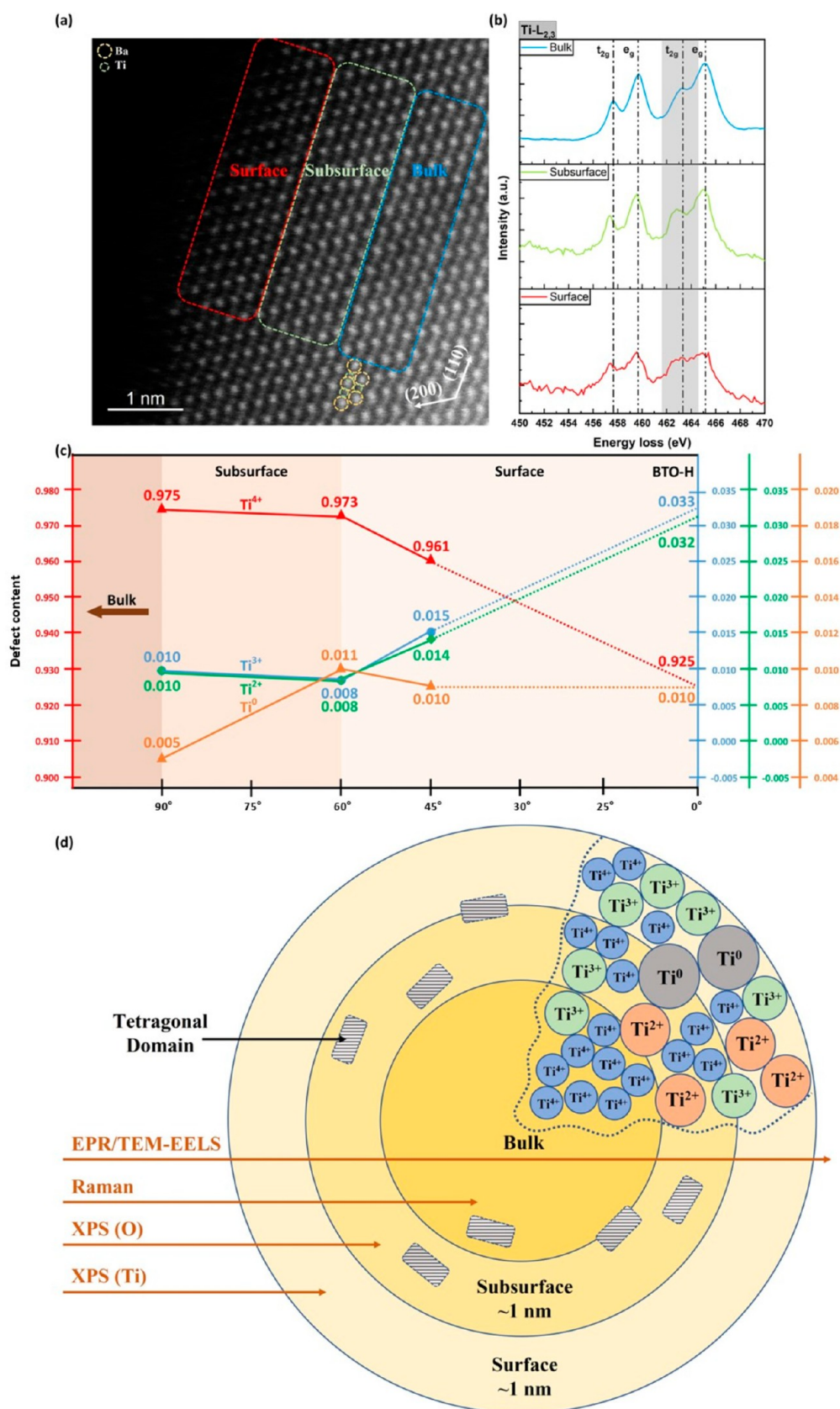


**Figure 3.** Analysis of defect concentrations as a function of depth. (a) HAADF-STEM image of surface, subsurface, and bulk regions of BTO-H. (b) EELS spectra of Ti L edges taken from the surface, subsurface and bulk regions of BTO-H. (c) Normalized ARXPS [Ti<sup>4-x</sup>] for BTO-H extrapolated to 90° (extreme surface). (d) Schematic of graded-reduction and analytical tool penetration depths from surface to subsurface to bulk for BTO-H based on data for (a-c).

ascribed to lattice oxygen ( $O_L$ ), nonlattice ionic oxygen associated with oxygen deficient ( $V_O^{\bullet\bullet}$ ) regions ( $O_V$ ), and adsorbed surface water and/or hydroxyl molecules ( $O_A$ ), respectively.<sup>10,17</sup> Concerning the critical  $O_V$  peak, this has been attributed to surface-adsorbed  $O^-$  ions, which have a reduced electron density.<sup>31</sup> Consequently, they alter the net electronic charge density and so can be detected by XPS although they often are ascribed nominally to oxygen vacancies.<sup>31</sup>

As shown in Figure S2 and Figure 2b,c as well as Table S3, the  $O_V/(O_L+O_V)$  ratio of BTO-H is 13.57 at%, which is distinctly higher than those of the other samples, viz., BTO-O (9.98 at%), BTO-N (10.27 at%), and BTO-A (11.03 at%), thus confirming the role of thermal reduction in the generation of structural defects in the form of charge-compensating  $Ti^{3+}$  (and possibly  $Ti^{2+}$ ) and  $V_O^{\bullet\bullet}$  (and possibly the other color centers  $V_O^\bullet$  and  $V_O^x$ ).

As shown in Figure 2d, the XPS spectra for the Ti 2p peaks at 458.10 eV (Ti 2p<sub>3/2</sub>) and 463.90 eV (Ti 2p<sub>1/2</sub>) confirm the dominant presence of  $Ti^{4+}$ .<sup>33</sup> Comparison of BTO-O with the other samples reveals that the Ti 2p peaks for the latter shifted to lower binding energies, which is indicative of the less-stable bonding configuration  $Ti^{4-x}\text{-O-Ti}^{4-x}$ . Although these shifts are consistent with reduced valences, the shifts are relatively small and within the uncertainty range of the reported binding energy measurements.<sup>41</sup> However, these shifts may indicate minor modification of the  $Ti^{4+}$  environment in the form of a small shift in its electron density. Although the most likely cause of this would be an increase in electronegativity upon reduction of  $Ti^{4+}$ , this is not supported by the values for  $Ti^{4+}$  (1.65) and  $Ti^{3+}$  (1.5). Consequently, this shift is consistent with the effect of oxygen vacancies, the absent ions of which have very high electro-negativity (3.65).

The depth distribution of structural defects was probed by HAADF-STEM, and these data were complemented by the determination of the corresponding chemical compositions using electron energy-loss spectroscopy (EELS). Figure 3a shows the atomic structure of a BTO-H nanoparticle viewed along the [002]/[110] orientation, with the Ba and Ti ionic columns clearly resolved. With the high-collection inner angle used for the HAADF-STEM imaging, the O ions are not visible.<sup>36</sup> The significantly lower contrast of the Ti ions in the surface relative to those in the subsurface may be attributed to the localized Ti orbital distortion and ionic displacement caused by the localized distortion associated with the  $Ti^{4+} \rightarrow Ti^{(4-x)+}$  reduction<sup>37</sup> and/or the structural distortion associated with the surface causes general ionic displacement, as reflected in the projected thickness.

Figure 3b shows the EELS spectra for the Ti-L<sub>2,3</sub> edges as a function of depth. The four peaks for the t<sub>2g</sub> and e<sub>g</sub> orbitals correspond to the electronic transitions from Ti 2p<sub>3/2</sub> (left pair, Ti-L<sub>3</sub>) and Ti 2p<sub>1/2</sub> (right pair, Ti-L<sub>2</sub>) bands.<sup>38</sup> Across the bulk  $\rightarrow$  subsurface, the t<sub>2g</sub> peak for the Ti-L<sub>2</sub> edge shifted to a lower energy loss, which indicates the existence of  $Ti^{(4-x)+}$ .<sup>11,39</sup> Further, the peaks become broader from the core to the surface, indicating increasing defect concentrations, particularly charge-compensating oxygen vacancies.<sup>28</sup> Across the subsurface  $\rightarrow$  surface, the principal difference is that the peaks are even broader, thus indicating that there is a significant increase in the defect concentrations across this interface. The observation from EELS is further underpinned by the results of the angle-resolved X-ray photoelectron spectroscopy (ARXPS), which are discussed immediately following.

Figure S5 illustrates the ARXPS spectra, which were used to understand the evolution of Ti valence state in BTO-H as a function of depth. The X-ray incident angles of 90°, 60°, and 45° differentiate probing depths by  $\sim 2\text{--}3$  nm. With lower incident angles, the distances of electrons traveling to the surface toward the detector are increased. Thus, the contributions of electrons from the deeper regions are minimized owing to the electron mean free path.<sup>40</sup> Significantly, the Ti 2p<sub>3/2</sub> spectra (three left peaks) reveal majority  $Ti^{4+}$  ( $458.7 \pm 0.15$  eV) and minority  $Ti^{3+}$  ( $456.8 \pm 0.15$  eV),  $Ti^{2+}$  ( $455.2 \pm 0.15$  eV), and  $Ti^0$  ( $453.9 \pm 0.15$  eV).<sup>40</sup>

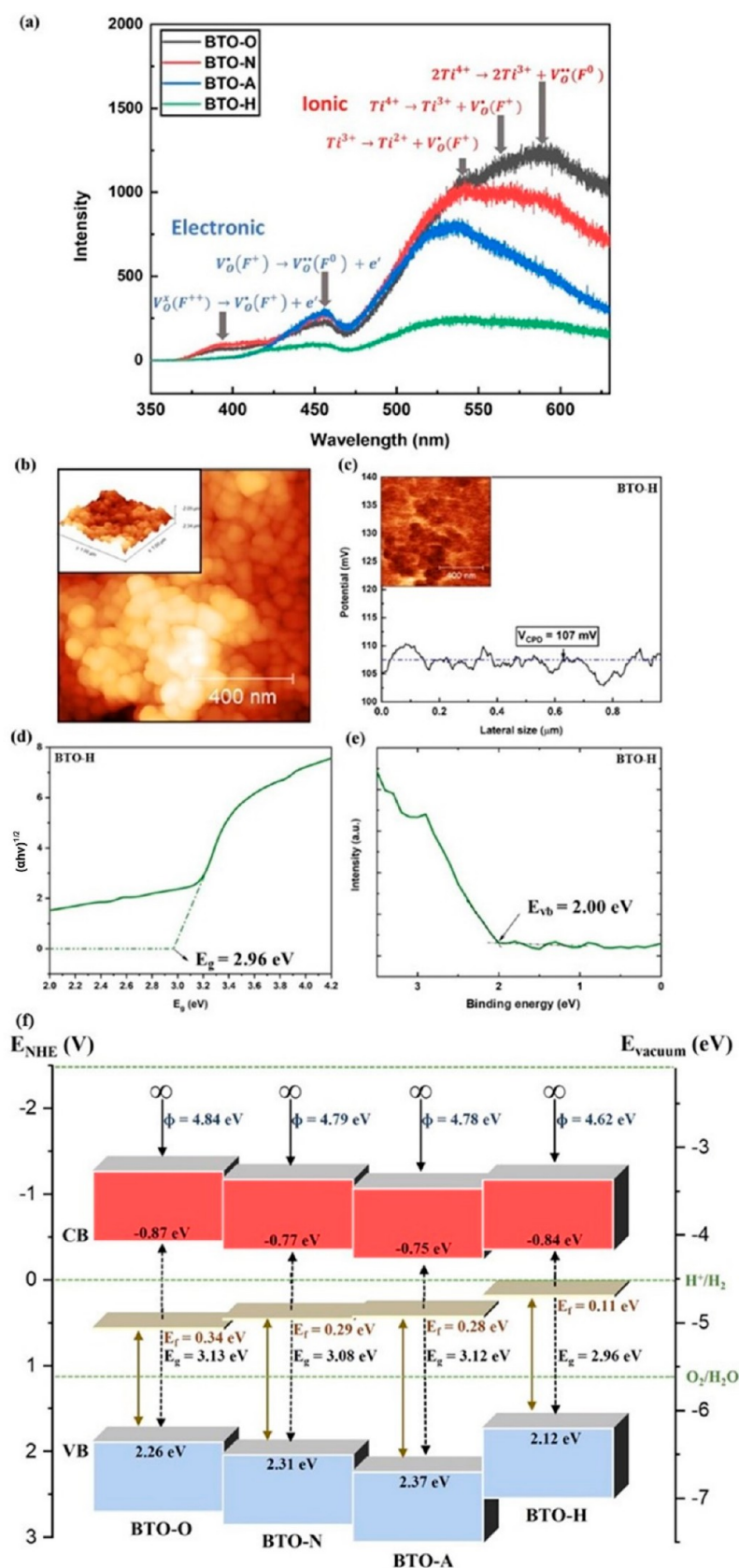
Figure 3c quantifies these data and extrapolates them to the absolute outer surface. This analysis allows two conclusions. First, in agreement with the EELS data, the inflection at 60° suggests the interface between the surface and subsurface, the former of which is estimated to be of a thickness  $\sim 1$  nm.<sup>35</sup> It is likely that there is a second inflection at a similar distance toward the bulk at a similar distance of  $\sim 1$  nm (viz., the subsurface thickness), which delineates the bulk/subsurface interface. However, this cannot be detected as the plot terminates by necessity at 90°. Second, the presence of  $Ti^0$  is limited effectively to the surface and subsurface. As the concentrations of the other three Ti ions are approximately constant, this suggests that the valence ratios are consistent throughout the bulk, thus demonstrating the high diffusivity of hydrogen in BTO and that the reduction is a bulk effect not a surface effect.

Figure 3d shows a schematic that combines the conclusions based on the EPR, EELS, and ARXPS data in terms of the concentration gradients for surface  $\rightarrow$  subsurface  $\rightarrow$  bulk. The presence of the oxygen-vacancy-stabilized tetragonal domains in the subsurface and bulk, the approximate surface and subsurface thicknesses, and the different analytical tool penetration depths also are shown.

The principal reason for the differences in compositions and concentrations between surface, subsurface, and bulk are suggested by the ordered nature of the bulk; the semioordered nature of the subsurface, which is the lattice termination; and the more disordered nature of the surface. In the present case, these effects are revealed by the origins of the  $Ti^{4+}$ ,  $Ti^{3+}$ ,  $Ti^{2+}$ , and  $Ti^0$ . Although these ions represent intrinsic defects, they also can be viewed as extrinsic surface defects owing to their origin, which would be one or more of the following:

- Adsorbates from unwashed raw materials
- Unwashed reaction products
- Products of inhomogeneous mixing
- Products of inhomogeneous reaction
- Establishment of concentration gradients during precipitation
- Establishment of concentration gradients during reaction
- Ions forced by stress from the bulk to the surface by segregation
- Chemisorbed ions in the subsurface that have detached from stress/repulsion and become physisorbed in the surface

Since EPR probes through the entire volume and Figure 2b demonstrates the presence of  $Ti^{3+}$ , this valence is confirmed as being present in the bulk. However, the presence of  $Ti^{2+}$  and  $Ti^0$  in the bulk cannot be probed by EPR as these valences are inactive.<sup>30</sup> These reductions are associated with progressive increases in the ionic radii<sup>25</sup> of  $Ti^{4+}$  (0.0745 nm),  $Ti^{3+}$  (0.081 nm), and  $Ti^{2+}$  (0.100 nm), terminating with the metallic radius of  $Ti^0$  (0.147 nm). The approximate doubling of the radius upon



**Figure 4.** Band structure characteristics of defective BTO nanoparticles. (a) PL spectra (identical pattern scales). (b) AFM topography of BTO-H drop-cast film. (c) Contact potential difference (CPD) of BTO-H drop-cast film by KPFM. (d) Kubelka–Munk plots from UV–vis reflectance spectrophotometry data for optical indirect band gap. (e) XPS valence band plots. (f) Resultant energy band diagrams.

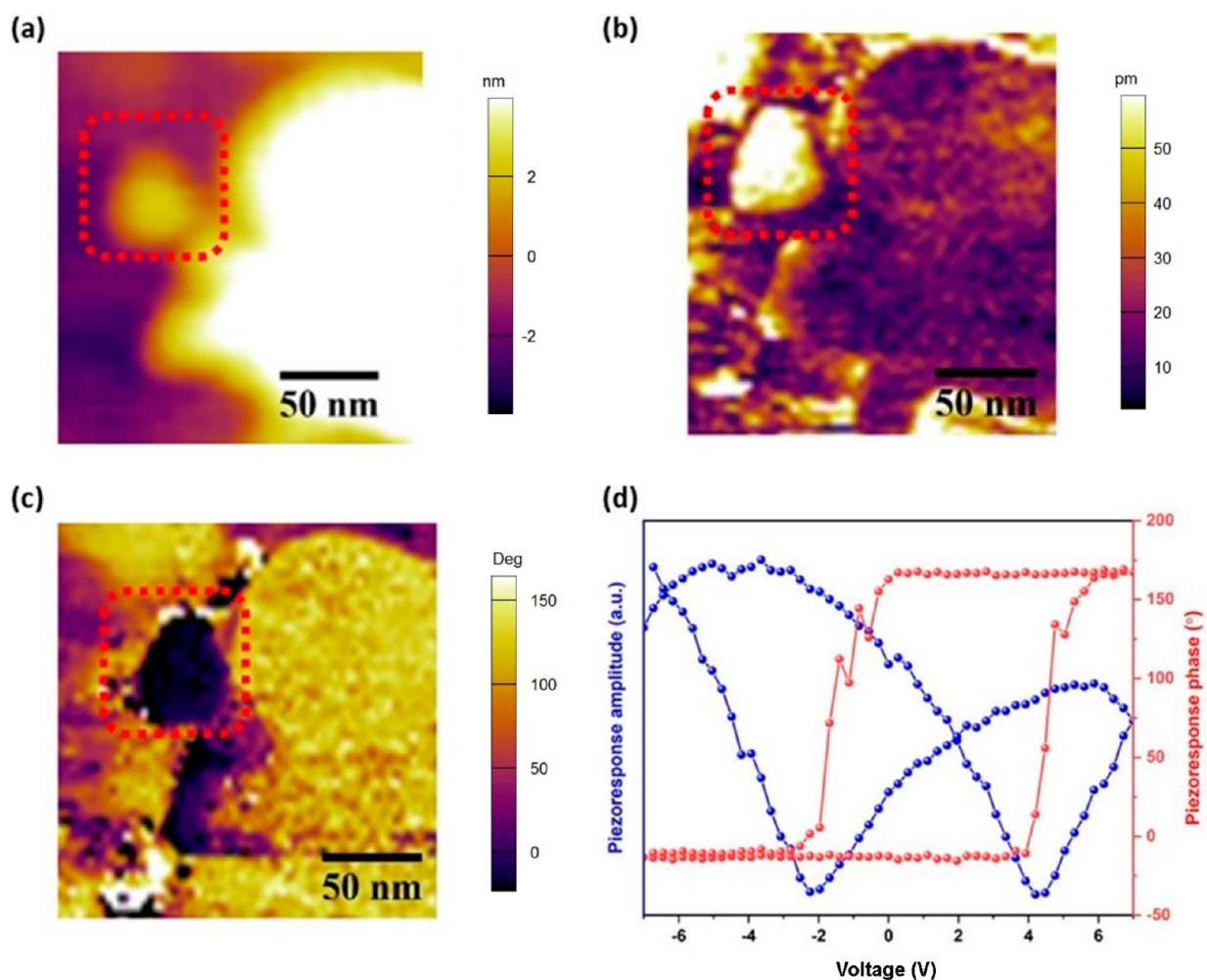


**Figure 5.** PFM results of defective BTO-H nanoparticles: (a) topography, (b) amplitude, and (c) phase images of a BTO-H nanoparticle. (d) Amplitude–voltage butterfly and phase–voltage hysteresis loops.

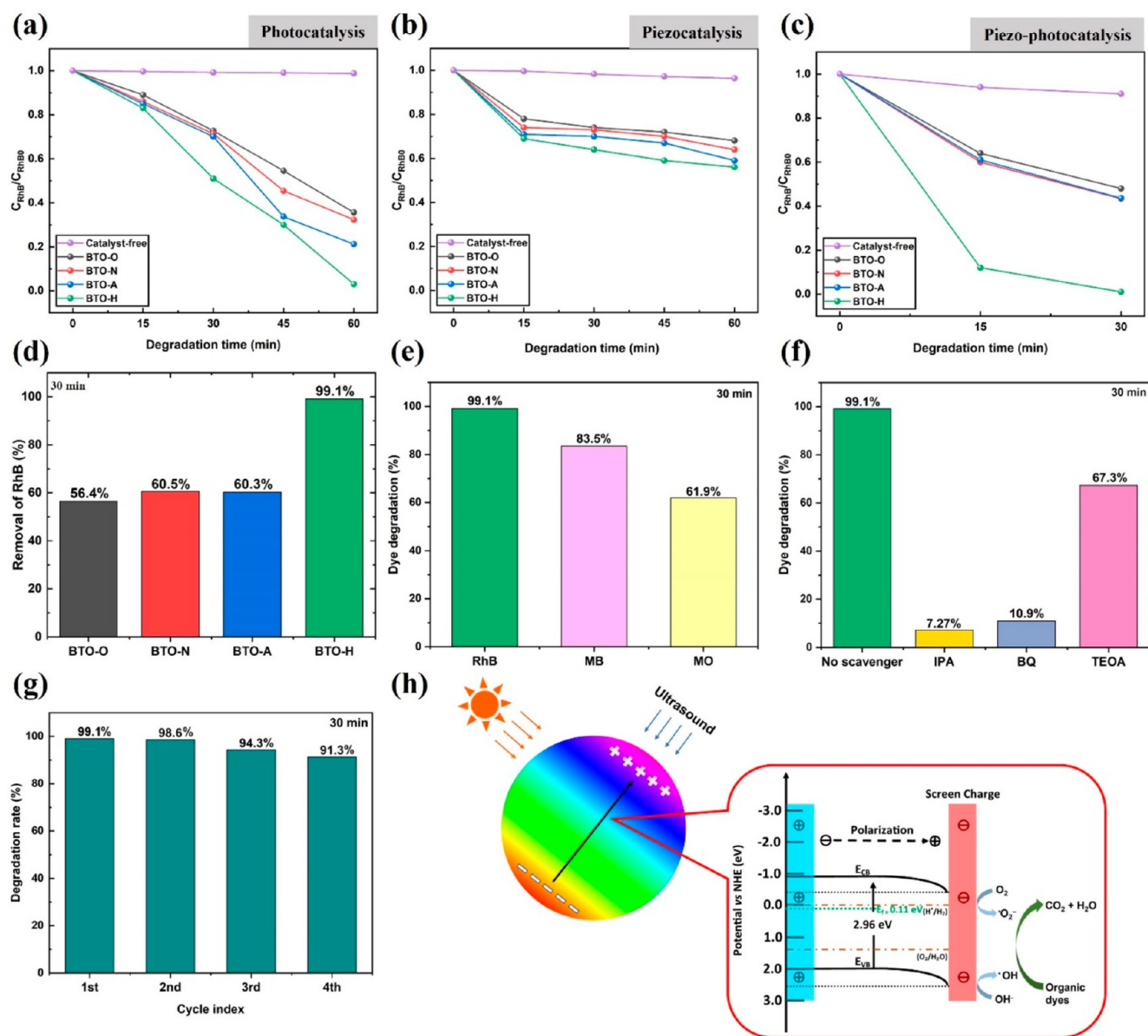
full  $\text{Ti}^{4+} \rightarrow \text{Ti}^0$  reduction is likely to be the cause of the limitation of the metal to the surface and subsurface.

Figure 4a shows the photoluminescence (PL) data for all four samples. These data confirm the existence of point defects, which facilitate energy transitions between ground and excited states and are associated with luminescent centers (color or F centers).<sup>42</sup> Since the peak intensities are inversely proportional to the electron–hole recombination rates, lower intensities reflect more significant effects. These rates of electron–hole recombination are controlled by the diffusion distance (i.e., particle size), the presence of trap states (i.e., defects), and the presence of heterojunctions (i.e., interfaces).<sup>35</sup> The two groupings of broad peaks are attributed to electronic defects associated with the near-band edge (color center transitions) and ionic defects associated with deep-level defect emissions (reductions that are charge-compensated by color center formation).<sup>43</sup> These two groupings are composed of the assignments of five transitions, where the inverse intensities are low for the ionic charge transitions and high for the electronic charge transitions. This bimodal distribution is expected as the amount of energy and time required to break bonds (to form oxygen vacancies) are greater than those to transfer an electron. Hence, the energy and time to create a color center ( $F^0(\text{V}_{\text{O}}^{\bullet\bullet})$ ,  $F^+(\text{V}_{\text{O}}^{\bullet})$ ,  $F^{2+}(\text{V}_{\text{O}}^{\bullet})$ ) are greater than those to add an electron ( $\text{V}_{\text{O}}^{\bullet\bullet} \rightarrow \text{V}_{\text{O}}^{\bullet}$ ,  $\text{V}_{\text{O}}^{\bullet} \rightarrow \text{V}_{\text{O}}^{\bullet}$ ). There are no effects from  $\text{Ti}^0$

because PL is inactive to metals as each exhibits a continuum of electronic states around the Fermi level, so no radiative transitions are possible between states above and below the Fermi level.

These transitions can be described in terms of Kröger–Vink notation applied to the potential defect equilibria. As the present work focuses on the passive reduction (oxygen partial pressure <21 vol %  $\text{O}_2$ ) and active reduction (chemical effect) of  $\text{BaTiO}_3$  to form  $\text{V}_{\text{O}}^{\bullet\bullet}$ , the defect equilibria are intrinsic and the possible charge compensation mechanisms for the formation of  $\text{V}_{\text{O}}^{\bullet\bullet}$  are ionic, electronic, or redox<sup>35,44</sup> (see Defect Equilibria, Supporting Information)).

In order to investigate the effects of the atmosphere on the corresponding electronic band structures, XPS was used to determine each gap between valence band (VB) and the Fermi level ( $E_f$ ). Additionally, the optical indirect band gap ( $E_g$ ) and the work function ( $\Phi$ ) were determined by UV–vis spectrophotometry and amplitude-modulated Kelvin probe force microscopy (AM-KPFM), respectively. Figure 4b illustrates the topography of the necessary BTO-H drop-cast film, which generated a contact potential difference ( $V_{\text{CPD}}$ ) as shown in Figure 4c. The value of 107 mV is significantly higher than that of the other samples (Figure S6), indicating enhanced adsorption of the free charges (i.e., piezoelectric potential), which were formed from the external strain, on the polar surface



**Figure 6.** Catalytic performance of defective BTO nanoparticles following 10 min sonication: (a) photodegradation of RhB as a function of time, (b) piezo-degradation of RhB as a function of time, and (c) piezo-photodegradation of RhB as a function of time. (d) Extent of piezo-photodegradation of RhB solution after UV irradiation for 30 min. Catalytic performance of BTO-H nanoparticles: (e) extent of piezo–piezo-photodegradation of RhB, MB, and MO solutions after UV irradiation for 30 min and (f) piezo-photodegradation efficiency of RhB solution with different quenchers after UV irradiation for 30 min (IPA = isopropyl alcohol, BQ = *P*-benzoquinone, TEOA = triethanolamine). (g) Reusability testing after piezo-photodegradation for four cycles (30 min/cycle). (h) Conceptual energy band diagram for charge separation and transfer in BTO-H under simultaneous UV and ultrasonic irradiation.

of the nanoparticles.<sup>11</sup> The resultant improved piezoelectric potential facilitates efficient surface reactions.

On the basis of these data (Figure 4b–e), the energy band levels were calculated (see Energy Band Level Calculations, Supporting Information), a schematic of which is shown in Figure 4f. The key outcomes of these data are that, for the increasing reduction from BTO-O to BTO-H, the  $E_g$  decreased from 3.13 to 2.96 eV and the  $E_f$  rose from 0.34 to 0.11 eV, which is in very close proximity to the  $H_2/H_2O$  redox potential (0.00 eV) for HER. The former ( $E_g$ ) is attributed to the abundant defect concentrations ( $Ti^{3+}$ ,  $Ti^{2+}$ ,  $Ti^0$ ,  $V_O^{\bullet\bullet}$ ), which are midgap states, that also act as catalytically active sites. When these midgap states are close to the CB (n-type) or close to the VB (p-

type), they represent shallow energy levels, thus effectively reducing the  $E_g$  and enhancing charge carrier separation by promoting the diffusion of charge carriers to the surface.<sup>44</sup> The latter ( $E_f$ ) is attributed to the effect of F centers. It is known that the  $E_f$  can be raised significantly by F centers, even to an energy above that of the conduction band minimum (CBM).<sup>35</sup> Consequently, the electrons are trapped near the CBM and so they are conducting and have high mobilities. In effect, the proximity of the increased  $E_f$  to the redox potential of HER in the defective BTO indicates that the band levels are consistent with effective water splitting.

In order to understand the effects of ultrasound vibration on the energy band gap and band alignments of BTO,

first-principles calculations based on density functional theory (DFT) simulations were undertaken. Periodic compressive and tensile strains associated resulting from ultrasound vibrations were simulated statically using negative and positive uniaxial strains,  $\eta$ , applied along the polar axis of tetragonal BTO (see DFT Simulations, Supporting Information). The maximal strain amplitude considered in the DFT simulations was 2%. Although this value is likely to be larger than experimentally achieved with ultrasound, it allowed for unambiguous determination of the piezocatalytic behaviors induced by uniaxial strain applied to BTO.

The local piezoelectric properties of defective BTO were characterized by piezoresponse force microscopy (PFM) working in dual AC resonance tracking mode (DART) in order to minimize cross-signaling between the topography, PFM amplitude, and phase. The nanoparticles were deposited on indium tin oxide (ITO)-coated glass substrates by drop-casting. Topography, amplitude, and phase image of the defective BTO-H are shown in Figure 5a–c, respectively. A nanoparticle with diameter size of approximately 40 nm can be observed with strong PFM amplitude and phase contrast. The dark contrast in the BTO-H phase image unambiguously indicates a polarization-down state prior to exposure to a strong DC electric field, which is consistent with the observed positive voltage offset shown in Figure 5a. The PFM amplitude-voltage butterfly curve and phase-voltage hysteresis loop of a typical BTO-H nanoparticle are shown in Figure 5d. The strong ferroelectric characteristics of the BTO-H are indicated by the nearly 180° phase switching, and the unequivocal piezoresponse is evidenced by the classical PFM amplitude butterfly loop. The asymmetric loops, which have a voltage offset of  $\sim 2$  V, suggest the presence of significant self-polarization.<sup>45</sup> This often originates from a stress gradient or an internal bias field owing to the nonuniform distribution of oxygen vacancies.<sup>46</sup> Figure 5d and Figure S7 reveal that all four samples exhibit such asymmetries and offsets in the PFM butterfly loops but they are more pronounced in BTO-H while those of the other three samples are similar.

## CATALYTIC ACTIVITY

Figure 6a shows the extent of RhB photodegradation, where all catalysts show photoactivity under UV light. These curves can be fit to the generally observed pseudo-first-order kinetics, which are described by eq 1:<sup>47</sup>

$$\ln\left(\frac{C}{C_0}\right) = -kt \quad (1)$$

where:

- $c_0$  = initial concentration of RhB solution
- $c$  = final concentration of RhB solution
- $k$  = rate constant
- $t$  = time

The catalytic performance with UV irradiation only is in the order BTO-O ( $k \sim 0.013$ ) < BTO-N ( $k \sim 0.014$ ) < BTO-A ( $k \sim 0.015$ ) < BTO-H ( $k \sim 0.026$ ) and the extent of catalytic degradation for BTO-H was  $\sim 99\%$  in 60 min.

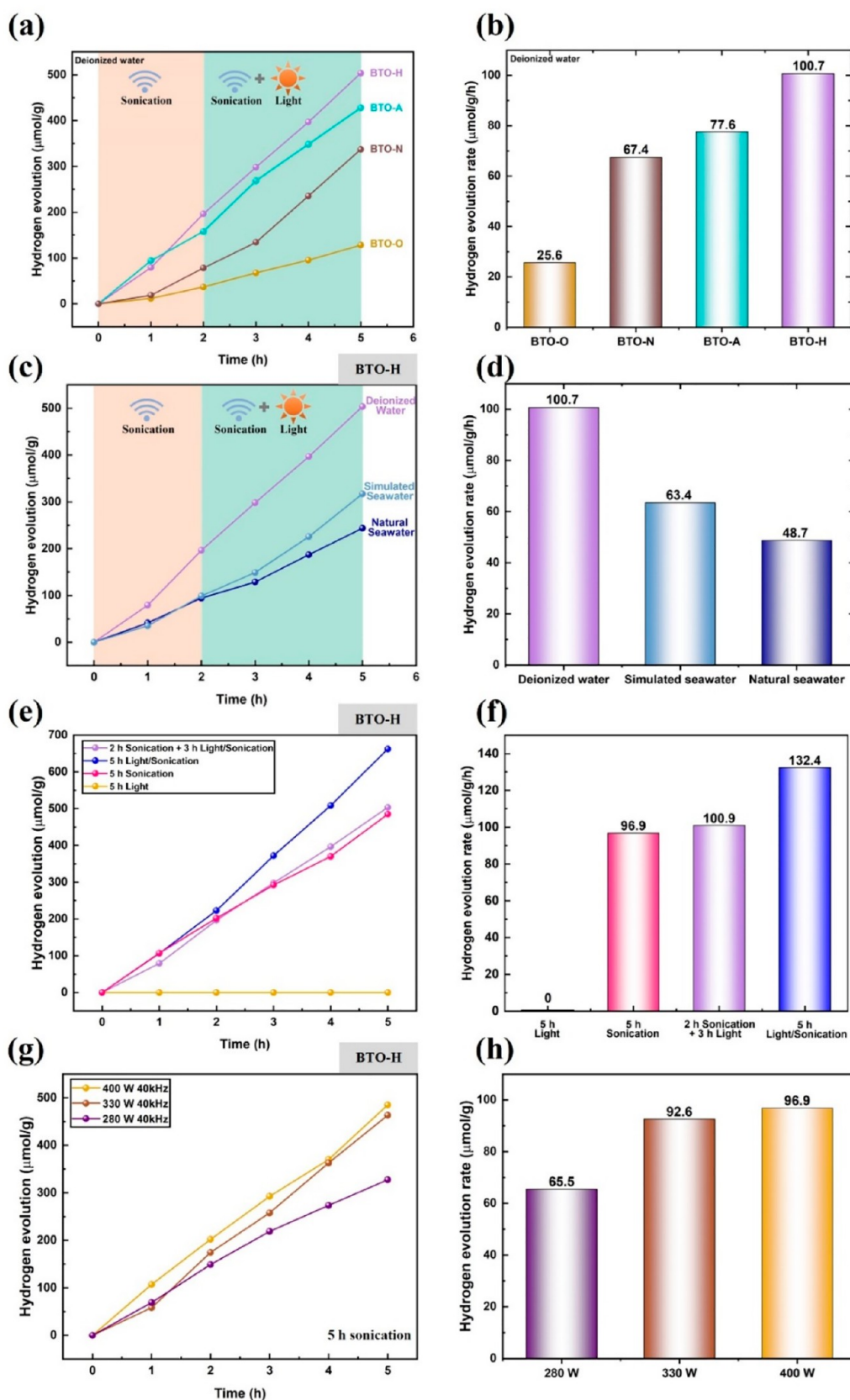
Figure 6b reveals that the capability of RhB degradation of BTO nanoparticles under only ultrasonic irradiation (40 kHz, 100 W) is highly consistent with that of photodegradation, i.e., BTO-H delivers the best piezocatalytic performance with a maximum degradation ratio of  $\sim 55\%$  in 60 min. As shown in

Figure 6c, the catalytic effect of all the BTO nanoparticles is greatly enhanced under simultaneous UV and ultrasonic (40 kHz, 100W) irradiation, compared to the monocatalysis. The degradation with BTO-H reached  $>99\%$  in 30 min, but the less defective samples reached a maximum of  $\sim 60\%$  within the same time frame. Figure 6d visualizes the superiority of BTO-H in RhB degradation at the fixed time point of 30 min. There are many materials factors that may affect these data, including phase assemblage, impurities (viz., heterojunction formation), crystallinity, crystallite size, electronic band alignment, recombination time, BET surface area,  $[V_{\text{O}}^{\bullet\bullet}]$ , and blockage of active sites.<sup>48</sup> Accordingly, the present work suggests that the catalytic performance (dye degradation) is associated with the following:

- The reduced  $E_g$  and shift in  $E_f$ , which are caused by increased defect concentrations ( $\text{Ti}^{3+}$ ,  $\text{Ti}^{2+}$ ,  $\text{Ti}^0$ ,  $V_{\text{O}}^{\bullet\bullet}$ ) and optimized by  $\text{H}_2$  reduction, result in band alignment that establishes conditions favorable for dye degradation
- The shallow energy level established by the high  $E_f$  and associated lowering of the CBM enhances charge carrier separation by promoting the diffusion of electrons to the surface, thereby reducing recombination with holes and facilitating higher carrier concentrations and efficient charge transfer across the grain surface.
- The increased BET surface area and associated  $[V_{\text{O}}^{\bullet\bullet}]$  are optimized by  $\text{H}_2$  reduction, thereby providing more active sites for catalytic reaction, although there may be mitigation by blockage of active sites by species dissolved in the water.
- The application of mechanical vibration leads to a displacement of charges (and possibly adsorbed species), thereby inducing the piezoelectric potential that facilitates surface reactions.
- The ultrasonic irradiation and resultant external stress induce the reduced band gap and band bending that shifts the conduction band closer to the HER band potential and the valence band further away from the OER band potential.
- It also is possible that multivalent Ti itself can act as a heterojunction structure to improve electron mobility and reduce charge transfer resistance, both of which are beneficial to the catalytic activity. As illustrated in Figure 3, such heterojunctions can take the form of a graded interface or a discrete series of interfaces at the surface, subsurface, and bulk.

The comparative testing using MB and MO dyes also showed substantial extents of degradation within the same time frame of 30 min, as illustrated in Figure 6e. These dyes were selected for the catalytic degradation owing to differences in the wavelengths of maximal visible light absorption relative to that of RhB. That is, RhB absorbs maximally in the green range at 554 nm while MB absorbs most strongly in the red range at 664 nm and MO absorbs most strongly in the blue range at 464 nm.<sup>48</sup> These data suggest that absorption may not be a serious limitation to the decomposition of a wide spectrum of organic contaminants of water purified by piezo-photocatalysis.

Figure 6f shows the effects of different reactive oxygen species (ROS) in the process of RhB piezo-photocatalytic degradation through introducing three scavengers: triethanolamine, TEOA; *P*-benzoquinone, BQ; and isopropyl alcohol, IPA. Previous work<sup>49</sup> has confirmed that these scavengers exhibit the respective capacities to quench ROS: TEOA for active holes ( $h^+$ ), BQ for the superoxide radical ( $\bullet\text{O}_2^-$ ), and the IPA for the



**Figure 7.** Effects of test conditions on  $\text{H}_2$  evolution by defective BTO: (a) data for deionized water, (b) rates for deionized water, (c) data for different waters, (d) rates for different waters, (e) data for different activation methods, (f) rates for different activation methods, (g) data for different piezocatalysis power levels, and (h) rates for different piezocatalysis power levels.

**Table 1.** Summary of pH and ICP-OES Elemental Analyses of Different Waters before and after Piezo-Photocatalytic H<sub>2</sub> Evolution

water type	before or after HER	pH	Na mg/L (ppm)	Cl mg/L (ppm)	K mg/L (ppm)	Mg mg/L (ppm)	Ca mg/L (ppm)	S mg/L (ppm)	C mg/L (ppm)
deionized water	before	7.44	0.00	0.00	0.00	0.00	0.00	0.00	0.00
simulated seawater		5.30	11,021	15,916	7.00	0.10	0.79	0.05	0.00
natural seawater	after	5.84	11,187	18,900	396.80	1,496.00	441.00	925.00	24.27
deionized water		8.38	0.26	0.16	0.00	0.00	0.00	0.00	0.00
simulated seawater		6.04	11,084	19,958	10.10	0.08	0.47	0.86	5.55
natural seawater		6.20	11,532	23,159	399.30	1,493.00	433.00	925.99	25.77

hydroxyl radical ( $\bullet\text{OH}$ ). The present data reveal an order in quenching effectiveness in the degradation of RhB, i.e., IPA ( $\bullet\text{OH}$ ) > BQ ( $\bullet\text{O}_2^-$ ) > TEOA ( $\text{h}^+$ ).

The photoelectric properties of the defective BTO nanoparticles were examined through the measurement of the photocurrent and electrochemical impedance spectroscopy (EIS). Figure S9a shows the photocurrent responses to irradiation, which suggest the efficiency of the separation and charge carrier transfer. When the light was switched on/off, the samples annealed under different atmospheres revealed enhanced photocurrents upon exposure. The photocurrent density of BTO-H is appreciably higher than those of the other samples. This is attributed to the enhanced oxygen vacancy concentration given in Figure 2c, which suppresses the fast recombination of photogenerated electrons and holes.<sup>61,62</sup> Figure S9b shows the Nyquist plots. Since the arc radius of the semicircular Nyquist plot for BTO-H is much smaller than those of the other samples, this shows that BTO-H exhibits smaller electron-transfer resistance and higher electrical conductivity. Both the photocurrent and EIS results are consistent with the catalytic activity and defect analyses (XPS, EPR, PL, TEM-EELS), demonstrating that BTO annealed under H<sub>2</sub> is efficient in reducing the recombination rates of photogenerated carriers.<sup>60</sup>

Figure 6g shows the stability and recyclability data for BTO-H in terms of four-cycle testing and the reduction in the degradation extent. The good cycling stability during piezo-photodegradation is similar to that of other studies on BTO done using both piezocatalysis<sup>24</sup> and piezo-photocatalysis.<sup>4,11</sup>

A schematic of the energy band diagram for the piezo-photocatalytic degradation of organic phases using defective BTO subjected to vibration and irradiation is shown in Figure 6h. Photocatalysis reactions are initiated by excitation from radiation energy ( $h\nu$ ) equal to or greater than the  $E_g$ . As a result, photogenerated electrons ( $e^-$ ) are promoted from the VB to the CB, leaving a hole ( $\text{h}^+$ ) in the VB. However, the application of ultrasonic stress can enhance the rapid generation of electrons further owing to two mechanisms.<sup>50</sup> First, electrons are generated from the high pressures ( $\sim 10^2$  MPa) caused by the collapse of ultrasound-induced cavitation bubbles in the solution. These pressures are sufficient to generate external ultrahigh temperatures locally on the grain surface, thereby readily exciting free electrons at the catalyst–water interface.<sup>50</sup> Second, electrons are generated in the bulk owing to the general internal thermal excitation induced by vibration.

The effectiveness of the electrons can be heightened by the strong piezoelectric effect of the BTO, which establishes an internal electrical field that facilitates the migration of excited electrons and holes to opposite surfaces, thereby establishing a surface potential that encourages the adsorption of dissociated

ions, such as  $\text{H}^+$  and  $\text{OH}^-$ , which can facilitate both ROS production and the water splitting.<sup>50</sup> Further, the accumulation of piezoelectrically induced charges on the opposite surfaces of the nanoparticles alters the density of states, thus resulting in bending of the surface band edges and establishing favorable band edges for the degradation of organic phases and water splitting. In particular, under a static deformation, the piezopotential drives the opposing mobile charges to continually accumulate on the two polar side to create a depolarization field, which counters the piezoelectric polarization effect and thus screen band bending.<sup>50</sup> Therefore, an alternating lattice strain is required, such as that produced by ultrasound, as the accompanied variation in the piezoelectric field enables the internal mobile charges to be in a metastable state rather than accumulating in an oriented manner, thereby preventing the band bending screen. While these concepts are relevant to stoichiometric BTO, the presence of oxygen vacancies in defective BTO further enhances catalysis through both adsorption of O<sub>2</sub> and capture of free electrons, which promoted the activation of O<sub>2</sub> to  $\bullet\text{O}_2^-$ . The present work and that of others<sup>10,51,52</sup> shows that  $\text{V}_\text{O}^{\bullet\bullet}$  play a critical role in enhancing the preceding processes. Wang et al.<sup>10</sup> confirmed that increasing  $[\text{V}_\text{O}^{\bullet\bullet}]$  could efficiently adsorb and activate O<sub>2</sub> on the surface of BTO and consequently enhance piezocatalytic activity, which is consistent with present work. Liu et al.<sup>51</sup> found that increasing  $[\text{V}_\text{O}^{\bullet\bullet}]$  provides more free surface charges and facilitates charge transfer in Na<sub>0.5</sub>Bi<sub>0.5</sub>TiO<sub>3</sub>, thereby improving the piezocatalytic activity. The increase in  $[\text{V}_\text{O}^{\bullet\bullet}]$  also promotes the adsorption of  $\text{O}_2^-$  and  $\bullet\text{OH}$  and activates the O–O bond and O–H bond to generate more ROS.

The H<sub>2</sub> evolution rates (HER) by piezocatalytic and piezo-photocatalytic activation of BTO also were investigated in the absence of sacrificial agent or cocatalyst. These data, which are for DI water and, for the first time, simulated and natural seawater, are shown in Figure 7a,b. Under the conditions of piezocatalysis for 2 h followed by piezo-photocatalysis for 3 h, the obtained HER of DI water follow the order: BTO-O < BTO-N < BTO-A < BTO-H, which is consistent with the dye degradation data in Figure 6a–d, again confirming the key role of the increasing defect concentrations ( $\text{Ti}^{3+}$ ,  $\text{Ti}^{2+}$ ,  $\text{Ti}^0$ ,  $\text{V}_\text{O}^{\bullet\bullet}$ ) and maximization by H<sub>2</sub> reduction. These data show that the H<sub>2</sub> evolution rates exhibit approximately linear relation with catalytic time, demonstrating that, at least over the time frame of 5 h, the H<sub>2</sub> production from DI water is constant, with a maximal rate of 100.7  $\mu\text{mol/g/h}$  (BTO-H), which is comparable to that of BiFeO<sub>3</sub> (124.1  $\mu\text{mol/g/h}$ )<sup>13</sup> and BaTiO<sub>3</sub> (159  $\mu\text{mol/g/h}$ ) nanoparticles.<sup>11</sup>

Parts c and d of Figure 7 show the effect of water type (DI water, simulated seawater, and natural seawater) on HER with BTO-H, revealing again linear H<sub>2</sub> evolution as a function of

time. However, the rates from seawaters are appreciably lower than that of the DI water, owing to the effects of the number of types and concentrations of dissolved ions. Whereas simulated seawater contains only dissolved NaCl at a standard concentration of 3.5 wt % (plus K contaminants), the natural seawater acquired from Coogee Beach, Sydney, Australia was of similar salinity but with a greater contamination level (Assessment of the salinity by [Na] is misleading owing to XPS data showing enhanced Na concentration on the surfaces of the separated nanoparticles. Assessment of the salinity by [Cl] should accommodate the assumption of the dissolution of K, Mg, and Ca chlorides, which results in [Cl] values within ~2% for simulated and natural seawaters.). It also contains suspended solids as well as dissolved inorganic and organic carbon. The ingredients in the natural seawater are given in Table 1, which provides the relevant concentrations before and after piezocatalytic H<sub>2</sub> evolution. In light of Na adsorption and retention on the nanoparticles, these data suggest that NaCl is the main factor behind these differences, where Na<sup>+</sup> would cause electron (*e*<sup>-</sup>) scavenging and Cl<sup>-</sup> would cause hole (*h*<sup>+</sup>) scavenging. The difference between simulated and natural seawater is attributed to the greater concentrations of K<sup>+</sup>, Mg<sup>2+</sup>, Ca<sup>2+</sup>, and SO<sub>4</sub><sup>2-</sup>.<sup>5</sup> Ji et al.<sup>53</sup> showed that Mg<sup>2+</sup> can reduce significantly the H<sub>2</sub> evolution. These findings were supported by those of Li et al.,<sup>53</sup> who showed that the chelation of Mg<sup>2+</sup> blocks the separation of photogenerated electron–hole excitons and induce charge redistribution, thereby negatively impacting on the photocatalytic performance.

More broadly, there are other extrinsic factors that can cause adverse effects on the HER of other types of water, such as wastewater, gray water, and industrial effluent, which may be acidic and basic. Ji et al.<sup>53</sup> also showed that the presence of lower concentrations of sulfite and sulfide ions could act as sacrificial agents, leading to higher HER activity. However, with higher concentrations of sulfite and sulfide ions, the HER was reduced. This was interpreted in terms of hindrance of electron migration to the surface owing to the adsorption of dissolved ions as well as the potential for precipitation of salts.<sup>53,54</sup> Another factor is the blockage of surface active sites by these ions as well as by suspended and dissolved species.<sup>5</sup> Solids suspended in seawater decrease light absorption by scattering and dissolved species may alter the refractive index and so increase reflection. These effects also can provide the energy to trigger biochemical reactions that can reduce the H<sub>2</sub> production as well.<sup>55</sup>

Table 1 also shows that the dissolution of NaCl shifted the pH from slightly basic to notably acidic, which might result from the formation of carbonic acid.<sup>55</sup> It is also confirmed that H<sub>2</sub> evolution resulted in consistent increases in the pH for all three types of water. The resultant decreases in [H<sup>+</sup>] would be likely to assist H<sub>2</sub> evolution owing to LeChatelier's principle,<sup>56</sup> where the chemical gradient would enhance H<sup>+</sup> dissolution.

Table 1 also reveals that [Na] is less than [Cl] in both seawaters, although they should be the same. This apparent anomaly was examined by multiple washing and XPS analysis of the adsorbates on the nanoparticles. These data are given in Table 2, and they reveal that [Na] is consistently greater than [Cl], which is the converse for the data for the corresponding solutions. Consequently, it is clear that Na is retained more readily as an adsorbate while the Cl is more readily removed by washing, which explains these two sets of oppositely differential data. This suggests that, if blockage of surface active sites is relevant then the reduction in H<sub>2</sub> evolution is a result of the effect of Na<sup>+</sup> rather than Cl<sup>-</sup>. This is consistent with the ζ

**Table 2. Summary of XPS Elemental Analyses of Different Powders after Piezo-Photocatalytic HER in Simulated Seawater or Natural Seawater**

seawater	washing	Ba (at%)	Ti (at%)	Na (at%)	Cl (at%)
simulated	10 min (15 mL)	10.82	12.66	41.53	34.98
	40 min (40 mL)	9.31	10.09	51.29	29.30
natural	10 min (15 mL)	31.04	16.99	41.18	10.78
	40 min (40 mL)	28.61	39.21	19.16	13.01

potential of BaTiO<sub>3</sub>, which is negative at almost all pH values.<sup>59</sup> These results suggest that the process, kinetics, and economics of seawater splitting can be manipulated through dilution, thereby reducing the effects of the dissolved species (and suspended solids), and the pH control, thereby increasing the H<sup>+</sup> solubility.

Parts e and f of Figure 7 show the effects of the activation methods for BTO-H, revealing the following features about the linear H<sub>2</sub> evolution rates:

- Photocatalytic HER of BTO is nearly inactive, which is attributed to the very rapid rate of electron–hole recombination observed in this material.
- Piezocatalytic HER of BTO is effective, giving H<sub>2</sub> evolution rates comparable to those of other BTO samples<sup>4,11</sup> and other materials, including BiFeO<sub>3</sub>,<sup>13</sup> ZnS,<sup>57</sup> MoS<sub>2</sub>,<sup>58</sup> etc. This is attributed to the following factors:
  - (1) The electrons generated from high pressures caused by the collapse of ultrasound-induced cavitation bubbles generate localized extremely high temperatures on the grain surface and so excite free charges to diffuse to the surface.
  - (2) The electrons generated in the bulk from vibration-induced thermal excitation are given sufficient energy to bridge the E<sub>g</sub>.
  - (3) The vibration-induced lowering of the E<sub>g</sub> from the ultrasound also facilitates the capacity of the electrons to bridge the E<sub>g</sub>.
  - (4) The high electron densities and rapid transfer rates deriving from (2) and (3) result in low electron–hole recombination rates.
  - (5) The electron accumulation deriving from (2) and (3) establish the band bending that facilitates the HER while suppressing the OER, as discussed subsequently.
- While the photocatalysis HER was 0% and the piezocatalysis HER was 100% (normalized), piezocatalysis HER increased the efficiency to 137%. This additional increment is attributed to the high electron densities, rapid transfer rates, and resultant low electron–hole recombination rates as described in (1–4) immediately above, which overcome the well-known rapid electron–hole recombination rates of perovskites. Thus, it is clear that piezocatalysis and photocatalysis are synergistic and so the whole is greater than the sum or its parts.

Figure S10, which reports the O<sub>2</sub>/N<sub>2</sub> molar ratio, provides indicative data for the effects of the activation methods on the OER. These data are tentative owing to the limited accuracy of O<sub>2</sub> volume measurement. Since the OER data in Figure S10 are consistent with the HER data in Figure 7e,f, this supports the conclusion that the OER data are relatively reliable. Also, the enhancement of the HER in Figure 7e,f and the suppression of

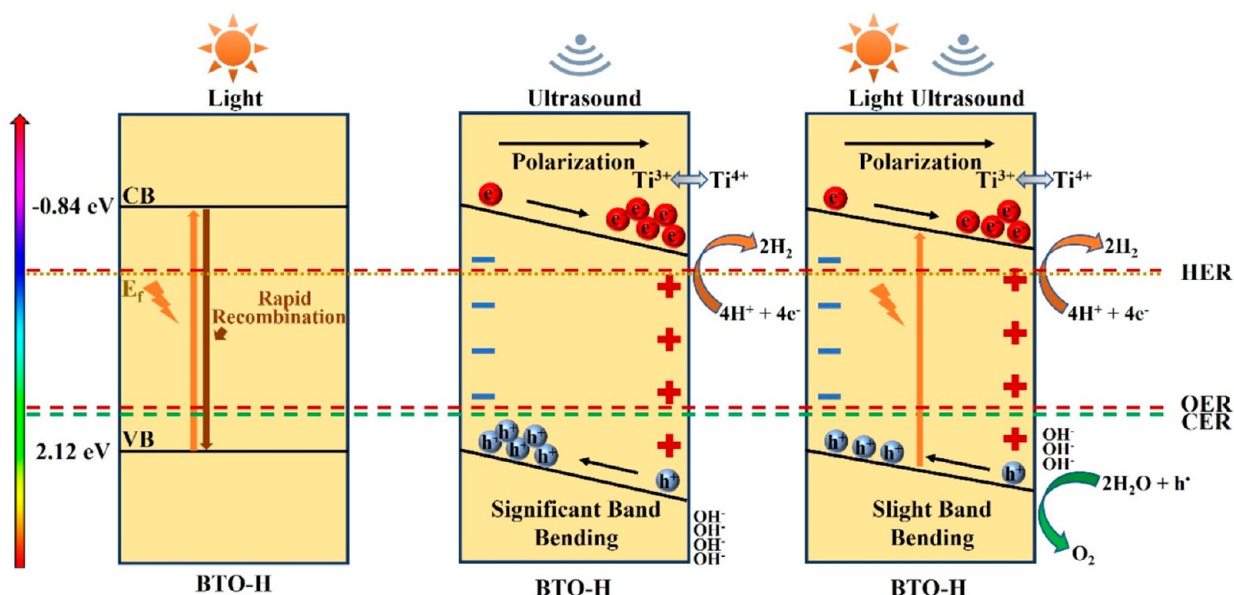


**Figure 8.** Schematic illustrations of band bending of defective BTO-H nanoparticles as a function of activation method.

the OER in Figure S10 are supported by the band bending indicated in the DFT simulations in Figure S8b. However, since OER occurred with piezo-photocatalysis, then this indicates that the band bending is relatively small. However, the HER can remain effective owing to the proximity of the  $E_f$  to the CB. In addition, Figure S11 reveals that the BTO-H nanoparticle has excellent recycle stability over four cycles.

Parts g and h of Figure 7 show the effects of ultrasound power alone on the  $H_2$  evolution rates for BTO-H, which are linear. These data reveal a positive relation between HER and ultrasound power. The governing relation between the power, which is a reflection of the external stress, and the HER, which is a reflection of the piezoelectric charge, is given by eq 2,<sup>13</sup>:

$$Q = d \cdot \sigma \quad (2)$$

where:

- $Q$  = piezoelectric charge per unit area
- $d$  = piezoelectric coefficient
- $\sigma$  = External stress

The data in Figure 7h is likely to reflect the effectiveness of the power level in deagglomeration, thereby exposing more surface active sites for piezocatalysis, where 280 W was less effective than the two higher power levels, which exhibited similar  $H_2$  evolution rates.

### ■ CATALYSIS REACTION MECHANISM

Figure 8 applies the preceding body of data to conceptualize the photocatalytic, piezocatalytic, and photopiezocatalytic  $H_2$  evolution reaction mechanisms:

- Photocatalysis: With defective BTO under visible light irradiation, electrons bridge the  $E_g$  and reach the CB, thus forming corresponding holes in the VB. However, these charge carriers rapidly recombine, thereby preventing HER and OER.
- Piezocatalysis: Defective BTO subjected to ultrasound alone benefits from the mechanical force directly excites the electrons to bridge the  $E_g$  owing to electron generation from bubble cavitation and thermal excitation, lowering of the  $E_g$  from vibration, resultant high electron densities and

rapid transfer rates, and significant band bending. The net electric field from the sum of the self-polarization and the stress-induced polarization, selectively attracts the electrons and holes, both of which accumulate and thus lead to band bending. Ultimately, this band bending facilitates the HER while suppressing the OER. In the absence of OER, change balance is maintained by the retention of  $OH^-$  ions from the splitting of  $H_2O$ , which raises the pH. Simultaneously, the tendency for the unstable surface  $Ti^{2+}$  and  $Ti^{3+}$  ions to oxidize is suppressed by the high electron densities.

- Piezo-photocatalysis: Defective BTO subjected to visible light irradiation and ultrasound together experiences benefits similar to those of piezocatalysis except that the process is enhanced through the contribution of photocatalysis. The inactivity of BTO to photocatalysis is overcome by the high electron densities, rapid transfer rates, and low electron–hole recombination rates established by piezocatalysis. However, the accumulated charge carrier densities on the band edge are reduced as some of these are utilized in photocatalysis. In this case, the extent of band bending is reduced, as evidenced by the occurrence of OER with piezo-photocatalysis. Fewer  $OH^-$  ions are produced as some of the  $H_2O$  is utilized in the OER, so the pH would be expected to increase less.

### ■ CONCLUSION

In the present work, defective  $BaTiO_3$  nanoparticles were prepared by heat-treatment of commercial BTO nanopowder under  $O_2$ ,  $N_2$ , Ar, or  $H_2$  in order to regulate the extent of reduction and achieve enhanced piezo-photocatalytic performance. A distorted structure was obtained after annealing in  $H_2$  and stabilized by the lattice expansion resulting from the  $Ti^{4+} \rightarrow Ti^{3+} \rightarrow Ti^{2+}$  multiple reductions, which were charge-compensated by oxygen vacancy formation. In addition, relatively large surface area, HER-favorable band structure and the substantial piezoresponse were proven in the BTO-H nanoparticles. The dye degradation through piezo-photocatalysis revealed that  $H_2$  reduction of BTO led to an effective

RhB degradation of 99% in 30 min. In addition, this highly defective BTO exhibited a very efficient H<sub>2</sub> evolution rate up to 132.4 μmol/g/h over DI water through piezo-photocatalysis. More importantly, this defective BTO nanoparticles also render remarkable seawater splitting capability with the HER rates of 63.4 μmol/g/h (simulated seawater) and 48.7 μmol/g/h (natural seawater). These differences were attributed largely to the role of the dissolved ions in seawater through their effects in irregular ROS generation, blockage of active sites by suspended and dissolved species, and/or triggered biochemical reactions. The present work discloses the initial report of piezo-photocatalysis of seawater splitting, representing a new and low-cost strategy for H<sub>2</sub> production through commercially available materials, potentially using large-scale green technologies, including mechanical vibrations deriving from wind energy and/or tidal energy (piezocatalysis) and sunlight (photocatalysis). Critically, these technologies can overcome the limited supplies of freshwater, the necessity of its purification, and make full utilization of abundant seawater and sunlight as well as geotechnical natural resources (large land masses, extensive shorelines, regular tidal patterns, and irregular wind patterns).

## EXPERIMENTAL SECTION

**Catalyst Preparation.** The raw BaTiO<sub>3</sub> nanopowders (BTO; reagent grade, 99 wt %) were purchased from Sigma-Aldrich. A sample of 1 g of powder was transferred to a loosely lidded alumina (Al<sub>2</sub>O<sub>3</sub>) crucible (1.5 mm H × 5 mm L × 2.5 mm W), placed in a Kanthal-wound muffle furnace, purged at room temperature for 1 h, heated at a rate of 5 °C/min, soaked at 800 °C for 12 h, and cooled naturally. The purging, heating, and cooling were conducted at a gas flow rate of 50 cm<sup>3</sup>/min using O<sub>2</sub> (BTO-O), N<sub>2</sub> (BTO-N), Ar (BTO-A), or 5 vol % H<sub>2</sub> + 95 vol % N<sub>2</sub> (BTO-H).

**Catalyst Characterization. Mineralogy.** The powders were characterized by X-ray diffraction (XRD; Aeris PANalytical Xpert Multipurpose X-ray diffractometer; Cu Kα, 45 kV, 40 mA, 0.026° 2θ step size, 29.27° 2θ step speed). These data were supplemented by those from laser Raman microspectroscopy (Raman; Renishaw in Via confocal Raman microscope, Renishaw; helium–neon green laser, diffraction grating 1800 grooves/mm). These data were analyzed using Renishaw WiRE 4.4 software, and the spectra were calibrated against the silicon peak at ~520 cm<sup>-1</sup>.

**Particulology.** The particle size distribution was determined by laser diffraction (Malvern Mastersizer 3000 laser diffraction particle size analyzer, Malvern). In a typical measurement, 100 mg of powder was dispersed in 100 mL of water using an ultrasonic bath for 10 min, after which the suspension analyzed during stirring at 2400 rpm. The specific surface area, pore volume, and average pore size were evaluated by the Brunauer–Emmett–Teller nitrogen adsorption method (BET; Quantachrome Autosorp 1MP; 0.1 g of sample, degassing for 1 h at 150 °C).

**Defect Chemistry.** The presence of defects was confirmed using electron paramagnetic resonance (EPR; Bruker EMX X-Band ESR Spectrometer; constant frequency at 9.8 GHz). The processing of the EPR spectra was performed using Bruker Xenon software. Qualitative analysis of defects was undertaken using photoluminescence spectroscopy (PL; Shimadzu spectro fluorophotometer RF-5301PC; excitation wavelength 325 nm, room temperature). Quantitative analysis of defects was conducted using X-ray photoelectron spectroscopy (XPS; Thermo Scientific ESCALAB 250Xi X-ray photoelectron spectrometer microprobe; 13 kV, 12 mA, 500 μm spot size). The angle-resolved XPS spectra were acquired using an UHV system (ARXPS; SPECS μ-Spot ARXPS, Mg anode, nonmonochromated, 12 kV, 200 W). In this method, thoria-coated tungsten filaments initially emit electrons that are accelerated onto an Mg anode, thereby causing X-ray emission that projects onto the sample surface. The intense photon from the X-ray excites an electron from an inner shell core level (s, p, and d electronic orbitals) owing to the excitation energy (1153.6 eV for the Mg anode)

of the sample, causing the transition of a photoelectron across the energy bands. The probing depth of ARXPS can be altered by changing the insertion angle between the X-ray source and sample surface. In the present work, characterization was conducted using insertion angles of 90° (maximal probe depth ~10 nm), 60° (~8.2 nm), and 45° (~7 nm). The nature of the electron excitation energy thus can be used for elemental analyses and the determination of the binding energies (elemental identification and valence changes) as a function of depth. The relative elemental concentrations were calculated by normalizing the individual element intensities to their individual atomic sensitivity factors (ASFs). The ARXPS spectra were calibrated on the basis of the assignment of the C–C sp<sup>3</sup> species to 285.0 eV owing to the observed charging of the BTO samples.

**Morphology.** Images of the nanoparticles were obtained by field emission scanning electron microscopy (FESEM; FEI Nova NanoSEM 230; 3 kV). Bright-field and high-resolution TEM images were taken using cold field emission transmission electron microscopy (FETEM; JEOL JEM-F200; 200 kV). High-resolution high-angle annular dark field (HAADF) images and STEM-EELS data were obtained by scanning transmission electron microscopy (STEM; JEOL Grand Arm 2; 300 kV), equipped with a Continuum image filter (Gatan).

**Band Levels.** The optical indirect (E<sub>g</sub>) was determined using the absorption spectra obtained from UV–vis spectrophotometry (UV–vis; PerkinElmer Lambda 1050 UV–visible spectrophotometer). The valence band level was determined using X-ray photoelectron spectroscopy and ultraviolet photoelectron spectroscopy (UPS; Thermo Scientific ESCALAB 250Xi X-ray photoelectron spectrometer microprobe; 13 kV, 12 mA, 500 μm spot size). The work function was determined using amplitude-modulated Kelvin probe force microscopy (KPFM), measuring using a Bruker Dimension ICON SPM equipped with a Nano Scope V controller. Platinum–silicide coated silicon probes (Bruker Nano Inc. SCM–PtSi) were used for all KPFM measurements. The scan size of the image was set to 1 μm with a pixel resolution of 256 samples/line. The lift height was set to 50 nm for all measurements. The work function of the tip was calibrated by scanning a freshly cleaved HOPG sample. The AFM images were processed using Gwyddion software.

**DFT Simulations.** First-principles calculations based on density functional theory (DFT) were performed in order to simulate and analyze the influence of uniaxial strain,  $\eta$ , on the optoelectronic and band alignment properties of ferroelectric BaTiO<sub>3</sub> (tetragonal phase, space group *P4mm*). Details are shown in the [Supporting Information \(SI\)](#).

**Piezoelectric Properties.** The local electromechanical properties of defective BTO nanoparticles were characterized by a commercial piezoresponse force microscopy (PFM) (Cypher S, Asylum research) working in dual AC resonance tracking mode (DART) to minimize the cross-talks with the morphology. Pt/Cr coated conductive probes (ElectriMulti 75G, BudgetSensors) with an average radius of <25 nm were used to acquire topography, PFM amplitude/phases images, and hysteresis loops of BTO nanoparticles under an AC bias of 0.5 V at ~350 Hz. The DC bias was applied through substrate for switching spectroscopy piezoresponse force microscopy (SSPFM) measurement.

**Piezocatalytic/Photocatalytic Applications. Dye Degradation.** The photocatalytic performance was examined by the photodegradation of aqueous solutions of Rhodamine B (RhB), methylene blue (MB), and methylene orange (MO). The solutions were prepared by dissolving RhB (R6626; Sigma-Aldrich; dye content ≥95 wt %), MB (M9140; Sigma-Aldrich; dye content ≥82 wt %), or MO (H301; Sigma-Aldrich; dye content ≥85 wt %) in deionized water at 10<sup>-5</sup> M concentration (0.0050 g of RhB, 0.0016 g of MB, or 0.0050 g of MO diluted in 500 mL of deionized water). Surface saturation of the powders was achieved by adding 30 mg of powder to 30 mL of dye solution in a 50 mL Pyrex beaker, followed by magnetic stirring at 300 rpm for 15 min under dark conditions in a light-obstructed black box. Each sample was exposed to 365 nm UV irradiation using a UV lamp (8 W, 3UV-38, UVP) while being magnetically stirred at 300 rpm for different times in the black box. The distance between the UV lamp and the solution surface was ~10 cm. The exposed solutions were separated from the powders by centrifuging at 5000 rpm for 10 min and

decanting, after which UV–vis testing of the supernatant was undertaken. The extents of RhB, MB, and MO degradation were determined from the relative changes in the intensities of the respective maximal peaks at 554 nm for RhB (green absorption), 664 nm for MB (red absorption), and 464 nm for MO (blue absorption). The piezocatalytic performance was examined using the same conditions as those for photocatalytic testing. But, instead of activation by UV irradiation, sonication was performed using an ultrasonic bath (FXP10; Unisonics; 40 kHz frequency, 100 W power) to activate the catalytic reaction. For the piezo-photocatalytic performance, both UV light and ultrasonic bath (FXP10; Unisonics; 40 kHz frequency, 100 W power) were used as trigger for the catalytic reaction.

**Hydrogen Evolution Reaction (HER).** For the piezocatalysis, the HER data were obtained using a previously described 150 mL off-line Pyrex top-illumination reactor, the opening of which was sealed with sleeve-stopper septum. For each run, 100 mg of the powder was added to 100 mL of DI water, simulated seawater (0.35 g of NaCl in 1 L of water), or natural seawater (obtained from Coogee Beach, Sydney, Australia), after which it was loaded into the reactor. The suspensions inside the cell then were dispersed using an ultrasonic bath (Hwashin, 100-510-240; 40 kHz, 400 W, 15 min). The gaseous contents of the cell then were removed by purging with argon at a gas flow rate of 15 cm<sup>3</sup>/min. The testing consisted of sonication of each suspension in the same ultrasonic batch but at power levels of 280, 330, or 400 W for 1–5 h. A gas sample of volume 1 mL generated above the solution was extracted at each hour during sonication by piercing the septum using a syringe. These samples subsequently were analyzed chemically by gas chromatography (Shimadzu GC 8A gas chromatograph). For the photocatalysis, the HER data were obtained as described for piezocatalysis except that, instead of sonication, irradiation was done using a 300 W xenon lamp with a 420 nm cutoff filter as the all-spectrum light source. For the piezo-photocatalysis, the HER data were obtained as described for piezocatalysis and photocatalysis but with combined sonication and irradiation. The generated gas was collected and analyzed using the same processes as those used for piezocatalysis and photocatalysis.

**Seawater Elemental Analyses.** Following piezo-photocatalysis, each dispersion was collected and the solution (DI-water-based, simulated-seawater-based, and natural seawater-based solutions) were separated from the powders by centrifuging at 5000 rpm for 10 min and decanting. The element analysis of each solution was done using inductively coupled plasma optical emission spectroscopy (ICP-OES, Avio 500, PerkinElmer). However, Cl ion detection was done by ion chromatography (Dionex ion chromatograph, ThermoFisher) and the total carbon content was detected using nondispersive infrared (NDIR) detection (Multi-NC 3100, Analytik Jena). The powders were separated into two groups, and each sample was mixed with 15 mL of DI water, ultrasonically dispersed for 5 min, centrifuged at 10,000 rpm for 10 min, and isolated by decanting. One of each pair of powders was mixed with 40 mL of DI water, ultrasonically dispersed for 5 min, centrifuged at 10,000 rpm for 10 min, and isolated by decanting. All of the powders were dried by placing in an oven at 100 °C for 4 h, followed by removal and natural cooling. All of the powders were analyzed elementally by X-ray photoelectron spectroscopy (XPS; Thermo Scientific ESCALAB 250Xi X-ray photoelectron spectrometer micropore; 13 kV, 12 mA, 500 μm spot size).

## ■ ASSOCIATED CONTENT

### Data Availability Statement

The data support the findings of this study are available from the corresponding author upon reasonable request.

### Supporting Information

The Supporting Information is available free of charge at <https://pubs.acs.org/doi/10.1021/acssuschemeng.2c06573>.

Tables of representative summary of investigations of photocatalytic hydrogen production from seawater, representative summary of ferroelectrics annealed under reducing atmospheres, Brunauer–Emmett–Teller

(BET) specific surface areas, pore volumes, and average pore sizes of defective BTO nanoparticles, comparative analysis of XPS O1s peaks and calculated peak ratios for defective BTO nanoparticles, and energy band gaps and levels, figures of crystal structures and representative lattice parameters, XRD Rietveld refinement data, particle size distribution, correlation between BET surface area and oxygen vacancy concentration, SEM, TEM, and EDS maps images, high-temperature EPR spectra of defective BTO nanoparticles, ARXPS Ti 2p spectra, Kubelka–Munk plots from UV–vis reflectance spectrophotometry data, PFM amplitudes and phase hysteresis loops, DFT calculated band structure characteristics of defective BTO nanoparticles, photoelectric current curves, EIS curves, measured O<sub>2</sub>/N<sub>2</sub> ratios, and recycling stability testing for piezo-photocatalytic HER performance, and discussions of additional experimental analysis (PDF)

## ■ AUTHOR INFORMATION

### Corresponding Authors

**Yue Jiang** – School of Materials Science and Engineering, UNSW Sydney, Sydney, NSW 2052, Australia; Email: [yue.jiang2@unsw.edu.au](mailto:yue.jiang2@unsw.edu.au)

**Danyang Wang** – School of Materials Science and Engineering, UNSW Sydney, Sydney, NSW 2052, Australia; [orcid.org/0000-0002-7883-8001](https://orcid.org/0000-0002-7883-8001); Email: [dy.wang@unsw.edu.au](mailto:dy.wang@unsw.edu.au)

**Charles C. Sorrell** – School of Materials Science and Engineering, UNSW Sydney, Sydney, NSW 2052, Australia; [orcid.org/0000-0002-1915-657X](https://orcid.org/0000-0002-1915-657X); Email: [c.sorrell@unsw.edu.au](mailto:c.sorrell@unsw.edu.au)

### Authors

**Cui Ying Toe** – Particles and Catalysis Research Group, School of Chemical Engineering, UNSW Sydney, Sydney, NSW 2052, Australia; [orcid.org/0000-0002-8480-5994](https://orcid.org/0000-0002-8480-5994)

**Sajjad S. Mofarah** – School of Materials Science and Engineering, UNSW Sydney, Sydney, NSW 2052, Australia; [orcid.org/0000-0002-4835-767X](https://orcid.org/0000-0002-4835-767X)

**Claudio Cazorla** – Departament de Física, Universitat Politècnica de Catalunya, Barcelona 08034, Spain; [orcid.org/0000-0002-6501-4513](https://orcid.org/0000-0002-6501-4513)

**Shery L.Y. Chang** – School of Materials Science and Engineering, UNSW Sydney, Sydney, NSW 2052, Australia; Electron Microscope Unit, Mark Wainwright Analytical Centre, UNSW Sydney, Sydney, NSW 2052, Australia; [orcid.org/0000-0001-7514-4584](https://orcid.org/0000-0001-7514-4584)

**Yanting Yin** – Flinders Institute for Nanoscale Science and Technology, Flinders University, Adelaide, South Australia 5042, Australia

**Qi Zhang** – School of Materials Science and Engineering, UNSW Sydney, Sydney, NSW 2052, Australia; [orcid.org/0000-0003-1940-8471](https://orcid.org/0000-0003-1940-8471)

**Sean Lim** – Electron Microscope Unit, Mark Wainwright Analytical Centre, UNSW Sydney, Sydney, NSW 2052, Australia

**Yin Yao** – Electron Microscope Unit, Mark Wainwright Analytical Centre, UNSW Sydney, Sydney, NSW 2052, Australia

**Ruoming Tian** – Electron Microscope Unit, Mark Wainwright Analytical Centre, UNSW Sydney, Sydney, NSW 2052, Australia

Yuan Wang – Centre for Advanced Materials and Industrial Chemistry (CAMIC), RMIT University, Melbourne, VIC 3000, Australia

Tasmia Zaman – School of Materials Science and Engineering, UNSW Sydney, Sydney, NSW 2052, Australia

Hamidreza Arandiyani – Centre for Advanced Materials and Industrial Chemistry (CAMIC), RMIT University, Melbourne, VIC 3000, Australia; Laboratory of Advanced Catalysis for Sustainability, School of Chemistry, University of Sydney, Sydney, NSW 2006, Australia; [orcid.org/0000-0001-5633-3945](https://orcid.org/0000-0001-5633-3945)

Gunther G. Andersson – Flinders Institute for Nanoscale Science and Technology, Flinders University, Adelaide, South Australia 5042, Australia; [orcid.org/0000-0001-5742-3037](https://orcid.org/0000-0001-5742-3037)

Jason Scott – Particles and Catalysis Research Group, School of Chemical Engineering, UNSW Sydney, Sydney, NSW 2052, Australia; [orcid.org/0000-0003-2395-2058](https://orcid.org/0000-0003-2395-2058)

Pramod Koshy – School of Materials Science and Engineering, UNSW Sydney, Sydney, NSW 2052, Australia

Complete contact information is available at:

<https://pubs.acs.org/10.1021/acssuschemeng.2c06573>

## Notes

The authors declare no competing financial interest.

## ACKNOWLEDGMENTS

The authors acknowledge the financial and infrastructural support from Tuition Fee Scholarship from UNSW Sydney and supplementary support from the China Scholarship Council, Electron Microscope Unit, Mark Wainwright Analytical Centre, UNSW Sydney, Spanish Ministry of Science, Innovation and Universities under the “Ramon y Cajal” fellowship RYC2018-024947-I, Microscopy Australia (formerly known as AMMRF), and the Australian National Fabrication Facility (ANFF) at Flinders University. The authors also wish to acknowledge the technical assistance of Dr. Dawei Zhang and Mr. Haotian Wen, School of Materials Science and Engineering, UNSW Sydney, for consultations and assistance with PFM and HAADF-STEM analysis.

## REFERENCES

- (1) Chang, J.; Wang, G.; Yang, Z.; Li, B.; Wang, Q.; Kuliiev, R.; Orlovskaya, N.; Gu, M.; Du, Y.; Wang, G.; Yang, Y. Dual-Doping and Synergism toward High-Performance Seawater Electrolysis. *Adv. Mater.* **2021**, *33* (33), 2101425.
- (2) LeValley, T. L.; Richard, A. R.; Fan, M. The progress in water gas shift and steam reforming hydrogen production technologies—A review. *Int. J. Hydrog. Energy* **2014**, *39* (30), 16983–17000.
- (3) Chen, H. L.; Lee, H. M.; Chen, S. H.; Chao, Y.; Chang, M. B. Review of plasma catalysis on hydrocarbon reforming for hydrogen production—interaction, integration, and prospects. *Appl. Catal. B Environ.* **2008**, *85* (1–2), 1–9.
- (4) Su, R.; Hsain, H. A.; Wu, M.; Zhang, D.; Hu, X.; Wang, Z.; Wang, X.; Li, F. T.; Chen, X.; Zhu, L.; Yang, Y.; Yang, Y.; Lou, X.; Pennycook, S. J. Nano-Ferroelectric for High Efficiency Overall Water Splitting under Ultrasonic Vibration. *Angew. Chem., Int. Ed.* **2019**, *58* (42), 15076–15081.
- (5) Jiang, S.; Liu, Y.; Qiu, H.; Su, C.; Shao, Z. High Selectivity Electrocatalysts for Oxygen Evolution Reaction and Anti-Chlorine Corrosion Strategies in Seawater Splitting. *Catalysts* **2022**, *12* (3), 261.
- (6) Simamora, A. J.; Hsiung, T. L.; Chang, F. C.; Yang, T. C.; Liao, C. Y.; Wang, H. P. Photocatalytic splitting of seawater and degradation of

methylene blue on CuO/nano TiO<sub>2</sub>. *Int. J. Hydrog. Energy* **2012**, *37* (18), 13855–13858.

(7) Peng, S. Q.; Liu, X. Y.; Ding, M.; Li, Y. X. Preparation of CdS-Pt/TiO<sub>2</sub> Composite and the properties for splitting sea water into hydrogen under visible light irradiation. *J. Mol. Catal.* **2013**, *27* (5), 459–466.

(8) Li, Q.; Li, X.; Yu, J. Surface and interface modification strategies of CdS-based photocatalysts. *Interface Sci. Technol.* **2020**, *31*, 313–348.

(9) Tu, S.; Guo, Y.; Zhang, Y.; Hu, C.; Zhang, T.; Ma, T.; Huang, H. Piezocatalysis and piezo-photocatalysis: catalysts classification and modification strategy, reaction mechanism, and practical application. *Adv. Funct. Mater.* **2020**, *30* (48), 2005158.

(10) Wang, P.; Li, X.; Fan, S.; Chen, X.; Qin, M.; Long, D.; Tadé, M. O.; Liu, S. Impact of oxygen vacancy occupancy on piezo-catalytic activity of BaTiO<sub>3</sub> nanobelt. *Appl. Catal. B: Environ.* **2020**, *279*, 119340.

(11) Su, R.; Wang, Z.; Zhu, L.; Pan, Y.; Zhang, D.; Wen, H.; Luo, Z.-D.; Li, L.; Li, F.-t.; Wu, M.; He, L.; Sharma, P.; Seidel, J. Strain-Engineered Nano-Ferroelectrics for High-Efficiency Piezocatalytic Overall Water Splitting. *Angew. Chem.* **2021**, *133* (29), 16155–16162.

(12) Hong, K. S.; Xu, H.; Konishi, H.; Li, X. Direct water splitting through vibrating piezoelectric microfibers in water. *J. Phys. Chem. Lett.* **2010**, *1* (6), 997–1002.

(13) Zhang, A.; Liu, Z.; Xie, B.; Lu, J.; Guo, K.; Ke, S.; Shu, L.; Fan, H. Vibration catalysis of eco-friendly Na<sub>0.5</sub>K<sub>0.5</sub>NbO<sub>3</sub>-based piezoelectric: an efficient phase boundary catalyst. *Appl. Catal. B: Environ.* **2020**, *279*, 119353.

(14) You, H.; Wu, Z.; Zhang, L.; Ying, Y.; Liu, Y.; Fei, L.; Chen, X.; Jia, Y.; Wang, Y.; Wang, F.; Ju, S.; Qiao, J.; Lam, C. H.; Huang, H. Harvesting the vibration energy of BiFeO<sub>3</sub> nanosheets for hydrogen evolution. *Angew. Chem.* **2019**, *131* (34), 11905–11910.

(15) Zhao, Z.; Wei, L.; Li, S.; Zhu, L.; Su, Y.; Liu, Y.; Bu, Y.; Lin, Y.; Liu, W.; Zhang, Z. Exclusive enhancement of catalytic activity in Bi<sub>0.5</sub>Na<sub>0.5</sub>TiO<sub>3</sub> nanostructures: new insights into the design of efficient piezocatalysts and piezo-photocatalysts. *J. Mater. Chem. A* **2020**, *8* (32), 16238–16245.

(16) Zhu, P.; Chen, Y.; Shi, J. Piezocatalytic tumor therapy by ultrasound-triggered and BaTiO<sub>3</sub>-mediated piezoelectricity. *Adv. Mater.* **2020**, *32* (29), 2001976.

(17) Wang, Y. C.; Wu, J. M. Effect of Controlled Oxygen Vacancy on H<sub>2</sub>-Production through the Piezocatalysis and Piezophotonics of Ferroelectric R3C ZnSnO<sub>3</sub> Nanowires. *Adv. Funct. Mater.* **2020**, *30* (5), 1907619.

(18) Xiao, H.; Dong, W.; Zhao, Q.; Wang, F.; Guo, Y. Visible/near-infrared light absorbed nano-ferroelectric for efficient photo-piezocatalytic water splitting and pollutants degradation. *J. Hazard. Mater.* **2021**, *416*, 125808.

(19) Zhu, D.; Liu, H.; Luo, H.; Sun, S.; Chen, J. Tetragonal phase and enhanced depolarization temperature in Ba-rich (Bi, Na)TiO<sub>3</sub>-BaTiO<sub>3</sub> lead-free piezoelectrics. *Ceram. Int.* **2020**, *46* (3), 3708–3714.

(20) Hagemann, H. J. Loss mechanisms and domain stabilisation in doped BaTiO<sub>3</sub>. *J. Phys. C* **1978**, *11* (15), 3333.

(21) Wu, J.; Xu, Q.; Lin, E.; Yuan, B.; Qin, N.; Thatikonda, S. K.; Bao, D. Insights into the role of ferroelectric polarization in piezocatalysis of nanocrystalline BaTiO<sub>3</sub>. *ACS Appl. Mater. Interfaces* **2018**, *10* (21), 17842–17849.

(22) Kim, D. H.; Lee, S. J.; Theerthagiri, J.; Choi, M.; Jung, J.; Yu, Y.; Im, K. S.; Jung, H. J.; Nam, S. Y.; Choi, M. Y. In-situ thermal phase transition and structural investigation of ferroelectric tetragonal barium titanate nanopowders with pseudo-cubic phase. *Chemosphere* **2021**, *283*, 131218.

(23) Fuentes, S.; Cespedes, F.; Munoz, P.; Chavez, E.; Padilla-Campos, L. Synthesis and structural characterization of nanocrystalline BaTiO<sub>3</sub> at various calcination temperatures. *J. Chil. Chem. Soc.* **2013**, *58* (4), 2077–2081.

(24) Wu, J.; Qin, N.; Bao, D. Effective enhancement of piezocatalytic activity of BaTiO<sub>3</sub> nanowires under ultrasonic vibration. *Nano Energy* **2018**, *45*, 44–51.

- (25) Shannon, R. D. Revised Effective Ionic Radii and Systematic Studies of Interatomic Distances in Halides and Chalcogenides. *Acta Crystallogr.* **1976**, *A32*, 751–767.
- (26) Tyunina, M.; Peräntie, J.; Kocourek, T.; Saukko, S.; Jantunen, H.; Jelinek, M.; Dejneka, A. Oxygen vacancy dipoles in strained epitaxial BaTiO<sub>3</sub> films. *Phys. Rev. Res.* **2020**, *2* (2), 023056.
- (27) Wu, K.; Sun, Y.; Liu, J.; Xiong, J.; Wu, J.; Zhang, J.; Fu, M.; Chen, L.; Huang, H.; Ye, D. Nonthermal plasma catalysis for toluene decomposition over BaTiO<sub>3</sub>-based catalysts by Ce doping at A-sites: The role of surface-reactive oxygen species. *J. Hazard Mater.* **2021**, *405*, 124156.
- (28) Baek, K.; Lee, S. Y.; Doh, S. G.; Kim, M.; Hyun, J. K. Axial oxygen vacancy-regulated microwave absorption in micron-sized tetragonal BaTiO<sub>3</sub> particles. *J. Mater. Chem. C* **2018**, *6* (36), 9749–9755.
- (29) Savchenko, D.; Vasin, A.; Kuz, O.; Verovsky, I.; Prokhorov, A.; Nazarov, A.; Lančok, J.; Kalabukhova, E. Role of the paramagnetic donor-like defects in the high n-type conductivity of the hydrogenated ZnO microparticles. *Sci. Rep.* **2020**, *10* (1), 1–9.
- (30) Wissel, K.; Dasgupta, S.; Benes, A.; Schoch, R.; Bauer, M.; Witte, R.; Fortes, A. D.; Erdem, E.; Rohrer, J.; Clemens, O. Developing intercalation based anode materials for fluoride-ion batteries: topochemical reduction of Sr<sub>2</sub>TiO<sub>3</sub>F<sub>2</sub> via a hydride based defluorination process. *J. Mater. Chem. A* **2018**, *6* (44), 22013–22026.
- (31) Jain, S.; Shah, J.; Negi, N. S.; Sharma, C.; Kotnala, R. K. Significance of interface barrier at electrode of hematite hydroelectric cell for generating ecpower by water splitting. *Int. J. Energy Res.* **2019**, *43* (9), 4743–4755.
- (32) Ji, M.; Kim, J. H.; Ryu, C. H.; Lee, Y. I. Synthesis of self-modified black BaTiO<sub>3-x</sub> nanoparticles and effect of oxygen vacancy for the expansion of piezocatalytic application. *Nano Energy* **2022**, *95*, 106993.
- (33) Jiang, Y.; Chen, W. F.; Koshy, P.; Sorrell, C. C. Enhanced photocatalytic performance of nanostructured TiO<sub>2</sub> thin films through combined effects of polymer conjugation and Mo-doping. *J. Mater. Sci.* **2019**, *54* (7), 5266–5279.
- (34) Jiang, Y.; Koshy, P.; Sorrell, C. C.; Wang, D. A Piezo Photocatalytic Process for the Production of Hydrogen from Water. Australian Provisional Patent Application No. 2022901443, 2022.
- (35) Zheng, X.; Mofarah, S. S.; Cazorla, C.; Daiyan, R.; Esmailpour, A. A.; Scott, J.; Yao, Y.; Lim, S.; Wong, V.; Chen, E. Y.; Arandiyani, H.; Koshy, P.; Sorrell, C. C. Decoupling the Impacts of Engineering Defects and Band Gap Alignment Mechanism on the Catalytic Performance of Holey 2D CeO<sub>2-x</sub> Based Heterojunctions. *Adv. Funct. Mater.* **2021**, *31* (38), 2103171.
- (36) Zhu, F.; Islam, M. S.; Zhou, L.; Gu, Z.; Liu, T.; Wang, X.; Luo, J.; Nan, C. W.; Mo, Y.; Ma, C. Single-atom-layer traps in a solid electrolyte for lithium batteries. *Nat. Commun.* **2020**, *11* (1), 1–9.
- (37) Mehmood, R.; Mofarah, S. S.; Chen, W. F.; Koshy, P.; Sorrell, C. C. Surface, subsurface, and bulk oxygen vacancies quantified by decoupling and deconvolution of the defect structure of redox-active nanocerium. *Inorg. Chem.* **2019**, *58* (9), 6016–6027.
- (38) Laskowski, R.; Blaha, P. Understanding the L<sub>2,3</sub> x-ray absorption spectra of early 3d transition elements. *Phys. Rev. B* **2010**, *82* (20), 205104.
- (39) Barzilay, M.; Qiu, T.; Rappe, A. M.; Ivry, Y. Epitaxial TiO<sub>x</sub> Surface in Ferroelectric BaTiO<sub>3</sub>: Native Structure and Dynamic Patterning at the Atomic Scale. *Adv. Funct. Mater.* **2020**, *30* (18), 1902549.
- (40) Wang, Y.; Shen, X.; Arandiyani, H.; Yin, Y.; Sun, F.; Chen, X.; Garbrecht, M.; Han, L.; Andersson, G. G.; Zhao, C. Tuning the surface energy density of non-stoichiometric LaCoO<sub>3</sub> perovskite for enhanced water oxidation. *J. Power Sources* **2020**, *478*, 228748.
- (41) Kramida, A.; Ralchenko, Y. NIST Standard Reference Database 78. *NIST Atomic Spectra Database*; National Institute of Standards and Technology: Gaithersburg, MD, 2022; p 10.
- (42) Wang, J.; Gürdal, E.; Horneber, A.; Dickreuter, S.; Kostcheev, S.; Meixner, A. J.; Fleischer, M.; Adam, P. M.; Zhang, D. Carrier recombination and plasmonic emission channels in metallic photoluminescence. *Nanoscale* **2018**, *10* (17), 8240–8245.
- (43) Vijayalakshmi, R.; Rajendran, V. Synthesis and characterization of cubic BaTiO<sub>3</sub> nanorods via facile hydrothermal method and their optical properties. *Dig. J. Nanomater. Bios.* **2010**, *5* (5), 511–517.
- (44) Bahmanrokh, G.; Cazorla, C.; Mofarah, S. S.; Shahmiri, R.; Yao, Y.; Ismail, I.; Chen, W. F.; Koshy, P.; Sorrell, C. C. Band gap engineering of Ce-doped anatase TiO<sub>2</sub> through solid solubility mechanisms and new defect equilibria formalism. *Nanoscale* **2020**, *12* (8), 4916–4934.
- (45) Zhang, Y.; Zheng, H.; Wang, X.; Li, H.; Wu, Y.; Zhang, Y.; Su, H.; Yuan, G. Enhanced photovoltaic properties of gradient calcium-doped BiFeO<sub>3</sub> films. *Ceram. Int.* **2020**, *46* (8), 10083–10088.
- (46) Guo, Y.; Guo, B.; Dong, W.; Li, H.; Liu, H. (2013). Evidence for oxygen vacancy or ferroelectric polarization induced switchable diode and photovoltaic effects in BiFeO<sub>3</sub> based thin films. *Nanotechnology* **2013**, *24* (27), 275201.
- (47) Hauch, A.; Tuqan, A. M.; Kibbi, N.; Geryes, S. Methylene blue discoloration by heated persulfate in aqueous solution. *Chem. Eng. J.* **2012**, *213*, 259–271.
- (48) Jiang, Y.; Chen, W. F.; Ma, H.; Ren, H.; Lim, S.; Lu, X.; Bahmanrokh, G.; Mofarah, S. S.; Wang, D.; Koshy, P.; Sorrell, C. C. Effect of Bi/Ti ratio on (Na<sub>0.5</sub>Bi<sub>0.5</sub>)TiO<sub>3</sub>/Bi<sub>4</sub>Ti<sub>3</sub>O<sub>12</sub> heterojunction formation and photocatalytic performance. *J. Environ. Chem. Eng.* **2021**, *9* (6), 106532.
- (49) Hayyan, M.; Hashim, M. A.; AlNashef, I. M. Superoxide ion: generation and chemical implications. *Chem. Rev.* **2016**, *116* (5), 3029–3085.
- (50) Wang, K.; Han, C.; Li, J.; Qiu, J.; Sunarso, J.; Liu, S. The Mechanism of Piezocatalysis: Energy Band Theory or Screening Charge Effect? *Angew. Chem.* **2022**, *134* (6), No. e202110429.
- (51) Liu, D. M.; Zhang, J. T.; Jin, C. C.; Chen, B. B.; Hu, J.; Zhu, R.; Wang, F. Insight into oxygen-vacancy regulation on piezocatalytic activity of (Bi<sub>1/2</sub>Na<sub>1/2</sub>)TiO<sub>3</sub> crystallites: Experiments and first-principles calculations. *Nano Energy* **2022**, *95*, 106975.
- (52) Li, L.; Ma, Y.; Chen, G.; Wang, J.; Wang, C. Oxygen-vacancy-enhanced piezo-photocatalytic performance of AgNbO<sub>3</sub>. *Scr. Mater.* **2022**, *206*, 114234.
- (53) Ji, S. M.; Jun, H.; Jang, J. S.; Son, H. C.; Borse, P. H.; Lee, J. S. Photocatalytic hydrogen production from natural seawater. *J. Photochem. Photobio. A Chem.* **2007**, *189* (1), 141–144.
- (54) Li, L.; Zhou, Z.; Li, L.; Zhuang, Z.; Bi, J.; Chen, J.; Yu, Y.; Yu, J. Thioether-functionalized 2D covalent organic framework featuring specific affinity to Au for photocatalytic hydrogen production from seawater. *ACS Sustain. Chem. Eng.* **2019**, *7* (22), 18574–18581.
- (55) Lee, C. T.; Hung, L. I.; Shih, Y. C.; Wu, J. C. S.; Wang, S. L.; Huang, C. W.; Nguyen, V. H. Solar hydrogen production from seawater splitting using mixed-valence titanium phosphite photocatalyst. *J. Environ. Chem. Eng.* **2021**, *9* (1), 104826.
- (56) Knox, K. Le Châtelier's Principle. *J. Chem. Educ.* **1985**, *62* (10), 863.
- (57) Feng, W.; Yuan, J.; Zhang, L.; Hu, W.; Wu, Z.; Wang, X.; Huang, X.; Liu, P.; Zhang, S. Atomically thin ZnS nanosheets: Facile synthesis and superior piezocatalytic H<sub>2</sub> production from pure H<sub>2</sub>O. *Appl. Catal. B Environ.* **2020**, *277*, 119250.
- (58) Su, Y.; Zhang, L.; Wang, W.; Li, X.; Zhang, Y.; Shao, D. Enhanced H<sub>2</sub> evolution based on ultrasound-assisted piezo-catalysis of modified MoS<sub>2</sub>. *J. Mater. Chem. A* **2018**, *6* (25), 11909–11915.
- (59) Luan, W.; Gao, L. Influence of pH value on properties of nanocrystalline BaTiO<sub>3</sub> powder. *Ceram. Int.* **2001**, *27* (6), 645–648.
- (60) He, F.; Meng, A.; Cheng, B.; Ho, W.; Yu, J. Enhanced photocatalytic H<sub>2</sub>-production activity of WO<sub>3</sub>/TiO<sub>2</sub> step-scheme heterojunction by graphene modification. *Chin. J. Catal.* **2020**, *41* (1), 9–20.
- (61) Liang, Z.; Bai, J.; Hao, L.; Shen, R.; Zhang, P.; Li, X. Photodeposition of NiS Cocatalysts on g-C<sub>3</sub>N<sub>4</sub> with Edge Grafting of 4-(1H-Imidazol-2-yl) Benzoic Acid for Highly Elevated Photocatalytic H<sub>2</sub> Evolution. *Adv. Sustain. Syst.* **2022**, 2200143.
- (62) Shen, R.; Zhang, L.; Li, N.; Lou, Z.; Ma, T.; Zhang, P.; Li, Y.; Li, X. W-N Bonds Precisely Boost Z-Scheme Interfacial Charge Transfer in

g-C<sub>3</sub>N<sub>4</sub>/WO<sub>3</sub> Heterojunctions for Enhanced Photocatalytic H<sub>2</sub> Evolution. *ACS Catal.* **2022**, *12* (16), 9994–10003.

(63) Li, J.; Sun, J.; Li, Z.; Meng, X. Recent advances in electrocatalysts for seawater splitting in hydrogen evolution reaction. *Int. J. Hydrogen Energy* **2022**, *47*, 29685.

## Recommended by ACS

### Structural Evolution and Durability of Ultrafine NiFe Phosphide Nanoparticle/Carbon Composite Films in Water Oxidation at High Current Densities

Yuan Sheng, Rong Xu, *et al.*

FEBRUARY 07, 2023

ACS APPLIED ENERGY MATERIALS

[READ !\[\]\(82ace3c1cdce20e5f8670b9f0a4207cd\_img.jpg\)](#)

### Porous Cuboidal SrNbO<sub>2</sub>N Crystals Grown on a Nb Substrate as an Active Photoanode for Neutral Seawater Splitting under Sunlight

Van-Huy Trinh and Jeongsuk Seo

JANUARY 20, 2023

ACS SUSTAINABLE CHEMISTRY & ENGINEERING

[READ !\[\]\(1ee9500f722bcabf6161b47e0c714cbe\_img.jpg\)](#)

### Advances in Carbon Dioxide Storage Projects: Assessment and Perspectives

Baolin Yang, Mohammed Dahiru Aminu, *et al.*

JANUARY 23, 2023

ENERGY & FUELS

[READ !\[\]\(588839c7e65636dffdd089c6ebe54d37\_img.jpg\)](#)

### Cu<sub>2</sub>O–Cu@Titanium Surface with Synergistic Performance for Nitrate-to-Ammonia Electrochemical Reduction

Marcelo Eduardo Chavez, Joan Ramon Morante, *et al.*

FEBRUARY 22, 2023

ACS SUSTAINABLE CHEMISTRY & ENGINEERING

[READ !\[\]\(a7069cde1de4d148f6375913b9bfe13b\_img.jpg\)](#)

[Get More Suggestions >](#)